LAWRENCE
LIVERMORE
NATIONAL
LABORATORY

UCRL-TR-219349

Acoustic Longitudinal Field NIF Optic Feature Detection Map Using Time-Reversal & MUSIC

Sean K. Lehman

February 27, 2006

This work was performed under the auspices of the U.S. Department of Energy by University of California, Lawrence Livermore National Laboratory under Contract W-7405-Eng-48.

Acoustic Longitudinal Field NIF Optic Feature Detection Map Using Time-Reversal & MUSIC

Sean K. Lehman

January 19, 2006

Abstract

We developed an ultrasonic longitudinal field time-reversal and **MU**ltiple **SI**gnal **C**lassification (MUSIC) based detection algorithm for identifying and mapping flaws in fused silica NIF optics. The algorithm requires a fully multistatic data set, that is one with multiple, independently operated, spatially diverse transducers, each transmitter of which, in succession, launches a pulse into the optic and the scattered signal measured and recorded at every receiver. We have successfully localized engineered "defects" larger than 1 mm in an optic. We confirmed detection and localization of 3 mm and 5 mm features in experimental data, and a 0.5 mm in simulated data with sufficiently high signal-to-noise ratio. We present the theory, experimental results, and simulated results.

UCRL-TR-219349

Contents

0 Executive Summary

Fully multistatic ultrasonic reflection mode data were collected on the fused silica NIF optic, measuring approximately 429 mm by 429 mm by 50 mm, pictured in Figure 1. The goal is to study the application of acoustic tomography techniques in detecting, localizing, and sizing features of sizes ranging from 0.1 mm to 5 mm within the optic. The glass is engineered with four machined hemispherical flaws measuring approximately 5 mm, 3 mm, 1 mm, and 0.5 mm, in diameter. A schematic of the optic, array, and flaws is presented in Figure 2(a). A time-reversal and **MU**ltiple **SI**gnal **C**lassification (MUSIC) [1, 2] based detection map was formed at 1.1 MHz from scattered longitudinal fields. The MUSIC algorithm is based upon the decomposition of the data into orthogonal *signal* and *noise* subspaces, where the scattered returns from the features are considered as existing within the signal subspace. Using this, points within the glass can be identified as sources of signal and, thus, the scatterers located. Size information is obtained based upon characteristics of the decomposition. Figure 2(b) shows the detection map with an 80% peak threshold applied. We emphasize this is not an acoustic *image* of the glass but rather a *detection map* with the flaws localized.

The algorithm was able to detect, localize, and successfully resolve the two largest flaws. We believe the returns from the two smallest flaws were lost in the measurement noise originating from a variety of sources including the electronics, switching circuitry, and transducer design. Additionally, the transducer array was offset to one side favoring the insonification of, and enhancing the backscatter from the two largest defects.

Our general conclusion is that a 1 MHz array consisting of contiguous point-like sources cannot provide sufficiently high signal-to-noise ratio (SNR) to measure the fields scattered from features smaller than 1 mm. We are confident the array design would be improved by using a higher frequency, 5 MHz for example, with an array of individual, spatially separated transducer elements each within their own housing. This would reduce element-to-element cross-talk and noise.

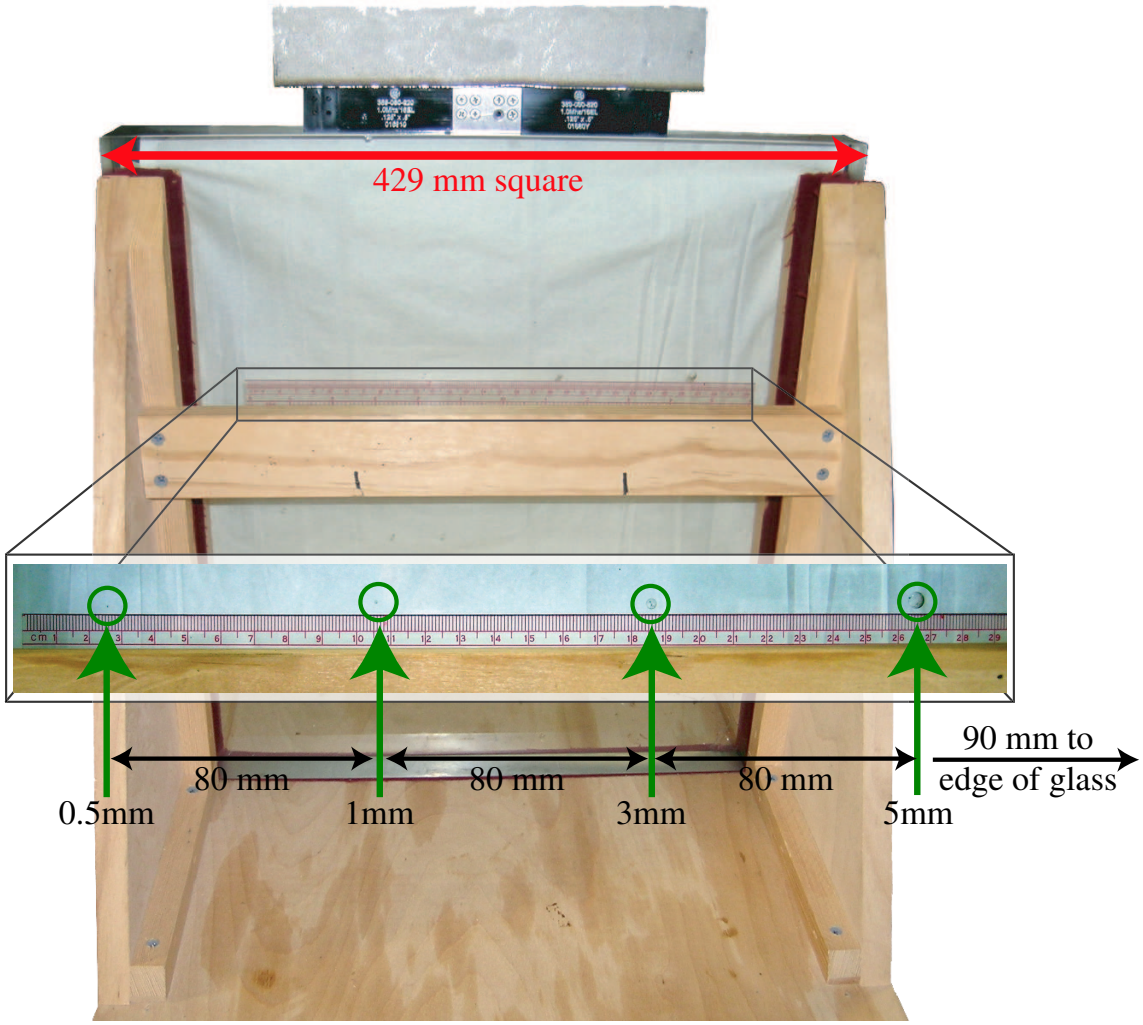

Figure 1: *Picture of fused silica NIF optic in mounting bracket. The ultrasonic transceiver array is on the top of the optic. The four engineered "defects" of sizes 0.5, 1, 3, and 5 millimeters are indicated. They are separated by 80 mm. The 5 mm defect is 90 mm from the right edge.*

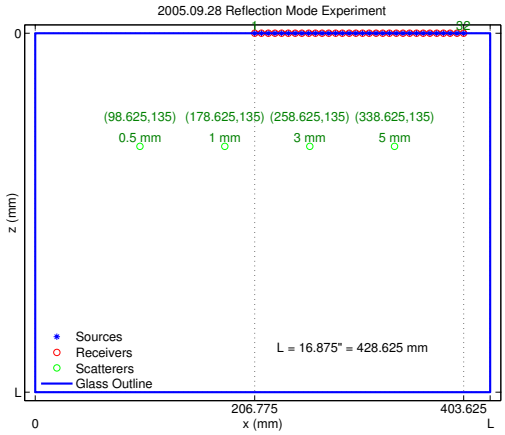

(a)

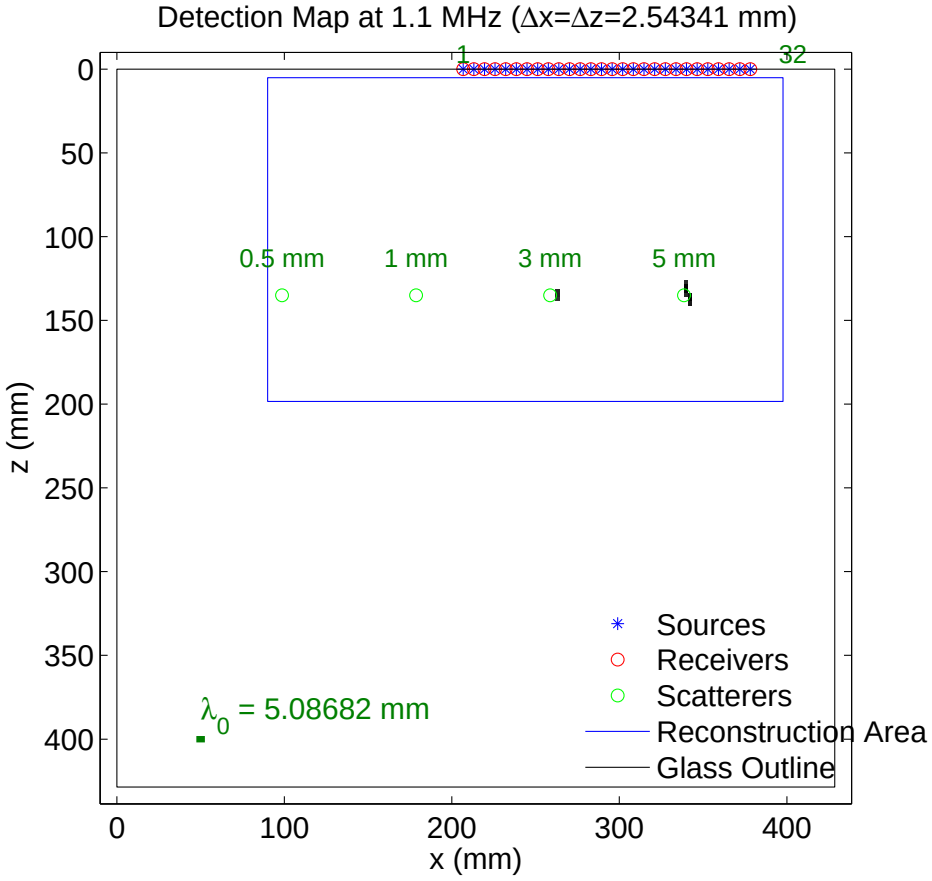

(b)

Figure 2: *(a) Schematic of fused silica NIF optic, multistatic reflection mode array placement, and defects. (b) Time-reversal & MUSIC based detection map with an 80% threshold applied. The resolution of the detection map is* $\lambda_0/2$ *or approximately 2.5 mm.*

1 Introduction

We developed an acoustic flaw detection map algorithm for a fused silica NIF optic. Our technique is to collect a fully multistatic (multiple spatially diverse receivers simultaneously measuring the scattered field from multiple spatially diverse sources) ultrasonic data set in either a reflection or transmission mode and process the measured scattered time series in a singular value decomposition [3] based time-reversal [4, 5, 6, 7, 8] algorithm. A **MU**ltiple **SI**gnal **C**lassification (MUSIC) based detection map [1, 2] was formed at a selected frequency, approximately 1 MHz, using longitudinal fields measured by a 32 element transceiver array.

We present the experimental results in the Executive Summary of Section 0 and in full detail in Section 2. As we believe we are signal-to-noise ratio (SNR) limited in the experiments, we describe a numerical analysis method using simulated data in Section 3. We analyze the SNR results in Section 4. We present our conclusions in Section 5.

The mathematical details of the time-reversal algorithm are presented in Appendices A and B. Typical simulated numerically generated backscattered time series are presented in Appendix D for various SNR levels. Corresponding feature detection results are shown in Appendix E.

2 Reflection Mode Experiment

A multistatic reflection mode experiment was performed using a 32 element 1 MHz array. The elements were 3.175 mm wide with a spacing of 6.35 mm. They were designed to have omnidirectional sound transmission and reception. The element-to-element isolation as rated by the manufacturer (GE Inspection Technologies) was approximately 40 dB. They were switched with a National Instruments SCXI 1160 matrix switch. We investigated several pulser/receiver combinations and concluded the UTEX UT340 was best for our purposes. We investigated methods various methods for reducing noise but had only limited success.

A schematic of the measurement geometry is presented in Figure 3. The time series were processed using the time-reversal algorithm of Appendix B at 1.1 MHz. The resulting singular value distribution is presented in Figure 4. We estimated a signal-to-noise ratio (SNR) of 10 dB. Because of the noise, the "zero" singular values are not identically zero as expected by the theory. However, the SNR is sufficient to identify clearly two scatterers as shown in Figure 4.

We formed a detection map of the scatterers using the pseudospectrum of Eqn. 56. We emphasize this is not an *image* of the scatterers but a *detection map* indicating where the algorithm located the features. This map is shown in Figure 5 where a threshold of 80% has been applied to the pseudospectrum.

The magnitude of the singular value is directly proportional to the scattering volume, that is, the size of the scatterer. Thus, the larger the singular value; the larger the scatterer. To extract, deterministically, scatterer size from a given singular value, the system must be calibrated. We did not perform this here.

The results show we have successfully located the two largest scatterers. The returns from the two smallest features were lost in the noise: we lacked sufficient SNR to detect them. The simulated study presented in Section 3, shows the system requires an SNR of at least 70 dB to detect, located, and size the smallest scatterer.

3 Signal-To-Noise Ratio Simulations

To study the signal-to-noise ratio (SNR) limitation further, we performed a series of simulated SNR tests using two operating modes:

- Full centered reflection from the top with a back wall reflection;
- Full centered reflection from the bottom with a top wall reflection.

These transducer geometries, presented in Figure 6, are fully multistatic reflection mode with 32 transceivers arranged to cover uniformly an entire side of the crystal. The reflecting wall is included via an expanded Green function,

$$G(\mathbf{r},\mathbf{r}') \quad = \quad G_0(\mathbf{r},\mathbf{r}') - G_0(\mathbf{r}, 2Z_0\hat{\mathbf{z}} - \mathbf{r}'), \tag{1}$$

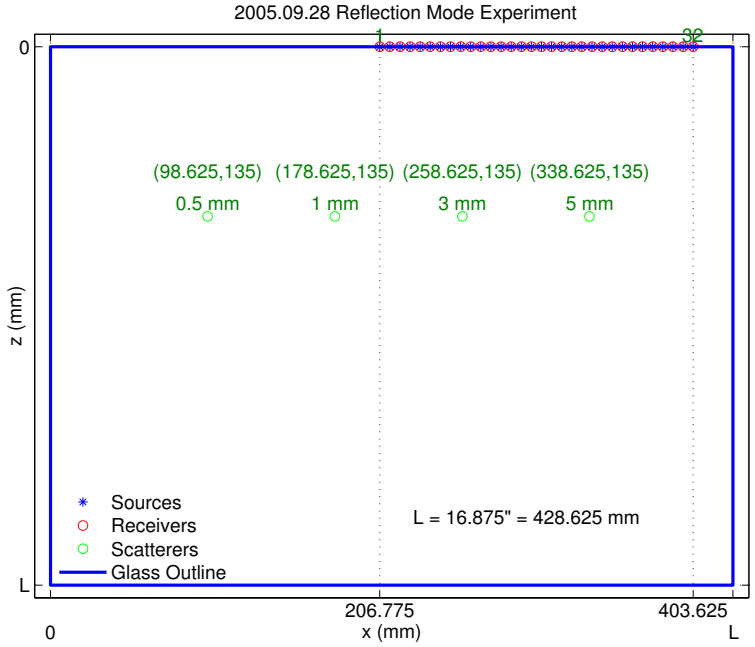

Figure 3: *2005/09/28 reflection mode experiment geometry. The transducer array was offset to one side favoring the insonification of and enhancing the backscatter from the two largest defects. The square optic is $L = 428.625$ mm on a side. The scatterer locations and sizes are indicated.*

where

$$G_0(\mathbf{r}, \mathbf{r}') \quad = \quad \frac{e^{ik_0(\omega)|\mathbf{r}-\mathbf{r}'|}}{4\pi|\mathbf{r}-\mathbf{r}'|}, \tag{2}$$

$\mathbf{r} \equiv (x, y, z)$, $\mathbf{r}' \equiv (x', y', z')$, $\hat{\mathbf{z}} \equiv (0, 0, 1)$, and the reflecting wall is located at $Z_0 = L$ when the array is on the top and $Z_0 = 0$ when the array is on the bottom. L is the optic, assumed to be square, side dimension.

For this study, we computed simulated measured scattered field time series using a Foldy-Lax scattering model ([9, 10, 11] and developed in a slightly different manner in [12]) and added zero-mean normally distributed random noise, $\mathcal{N}(0, \sigma_N)$ with a variance computed using:

$$\sigma_N \quad \equiv \quad \max_{m,n} \left(\left| \psi^{scat}(\mathbf{R}_m^r, \mathbf{R}_n^t, t) \right| \right) 10^{-\mathrm{SNR}/20}, \tag{3}$$

where SNR is the desired signal-to-noise ratio and $\max_{m,n} \left(|\psi^{scat}(\mathbf{R}_m^r, \mathbf{R}_n^t, t)| \right)$ is the maximum value of the magnitude of the scattered field over all source/receiver (m indexes the receivers; n the sources) combinations and all time. This results in the signal-to-noise ratio being defined as

$$\mathrm{SNR} \quad \equiv \quad 20 \log_{10} \left(\frac{\max_{m,n} \left(|\psi^{scat}(\mathbf{R}_m^r, \mathbf{R}_n^t, t)| \right)}{\sigma_N} \right). \tag{4}$$

Explicitly, we ran our time-reversal algorithm on

$$\psi^{scat}(\mathbf{R}_m^r, \mathbf{R}_n^t, t) + \mathcal{N}(0, \sigma_N), \tag{5}$$

with SNR values of infinity (no noise), and 10 through 80.

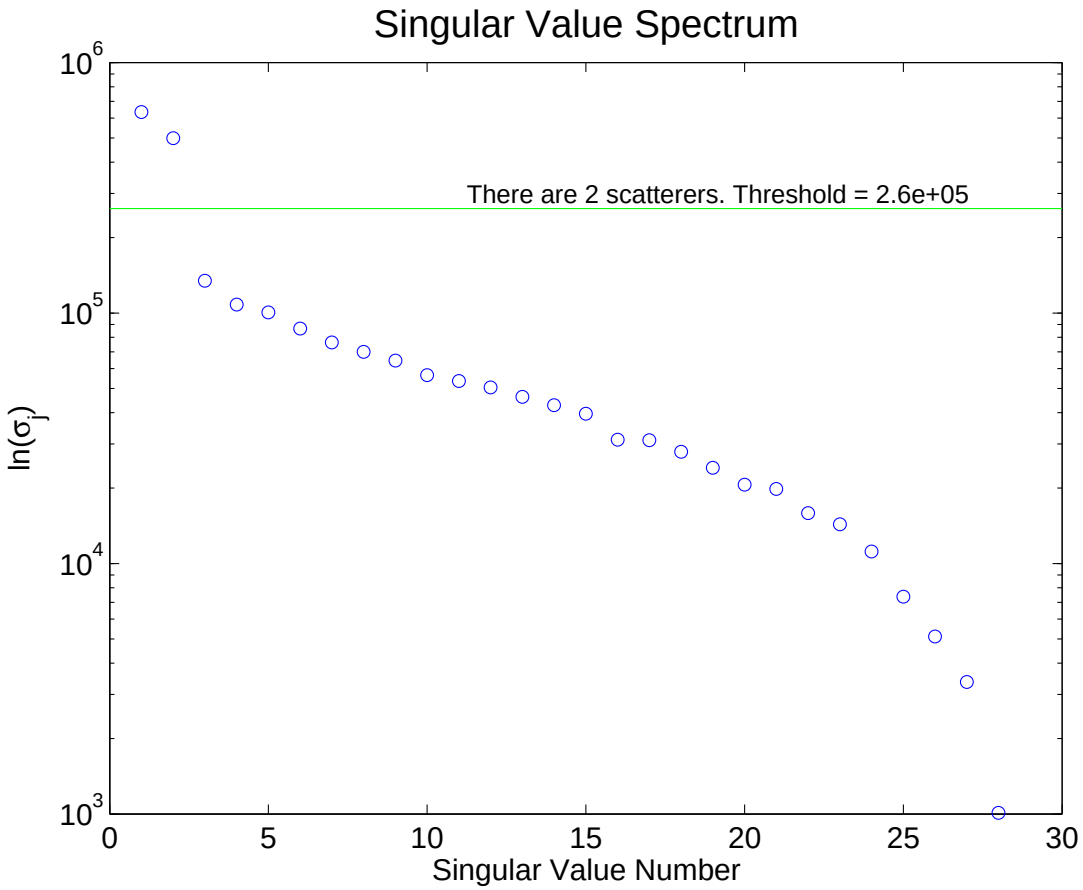

Figure 4: *Time-reversal singular value distribution. The distinct break in the distribution indicates where the threshold between the non-zero and "zero" singular values was made. There are clearly two singular values which stand out indicating there are two distinct scatterers.*

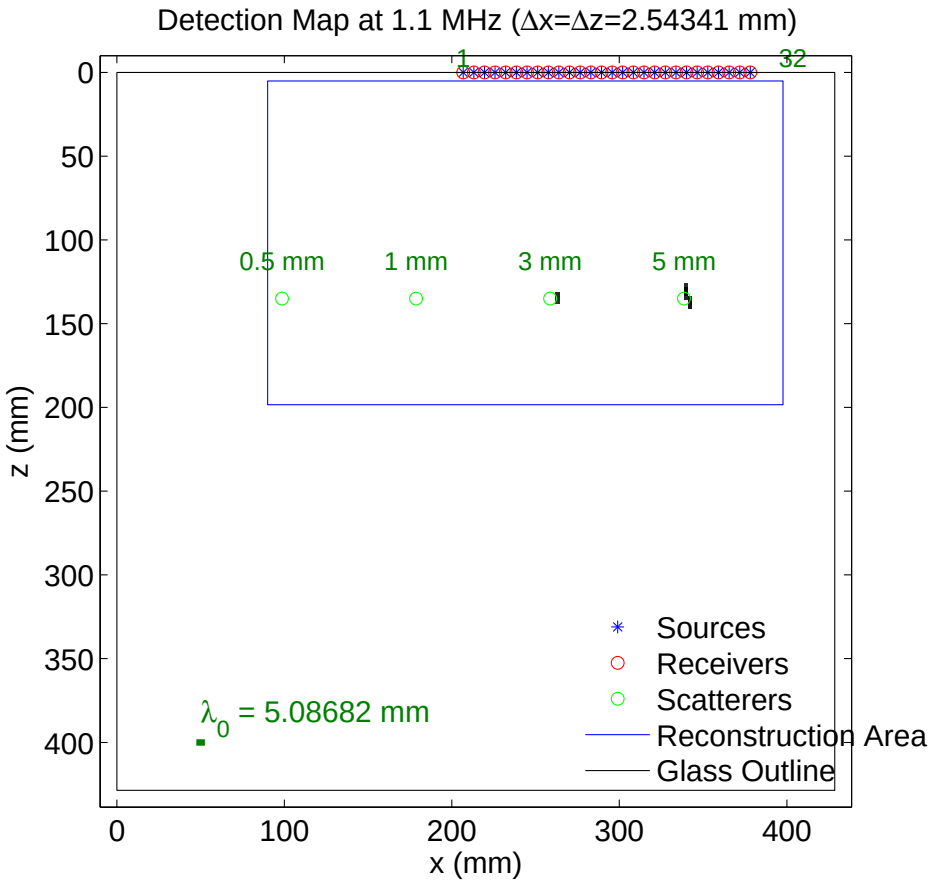

Figure 5: *Time-reversal & MUSIC based detection map with an 80% threshold applied. The resolution of the detection map is $\lambda_0/2$ or approximately 2.5 mm. We successfully detected and located the 3 and 5 mm features but were unable to identify the 1 mm and 0.5 mm features due to insufficient SNR. We estimate the SNR of the measured data set to be 10 dB. Our simulated analysis shows we require at least 70 dB to detect the 0.5 mm feature.*

We present our results as singular values of the multistatic data matrix as a function of SNR. We compare these results with the theoretical scatterer singular values computed via

$$\begin{aligned} g_r(\mathbf{r}) &\equiv [G(\mathbf{R}_1^r, \mathbf{r}),\ G(\mathbf{R}_2^r, \mathbf{r}),\ \cdots, G(\mathbf{R}_M^r, \mathbf{r})]^T, \\ g_t(\mathbf{r}) &\equiv P(\omega)\left[G(\mathbf{r}, \mathbf{R}_1^t),\ G(\mathbf{r}, \mathbf{R}_2^t),\ \cdots,\ G(\mathbf{r}, \mathbf{R}_N^t)\right]^T, \\ \sigma_j &= k_0^2(\omega)\ |\tau_j|\ \|g_t(\mathbf{X}_j)\|\ \|g_r(\mathbf{X}_j)\|. \end{aligned}$$

where there are M receivers, N transmitters, $\{\mathbf{R}_m^r\}_{m=1}^M$ are the receiver locations, $\{\mathbf{R}_n^t\}_{n=1}^N$ are the transmitter locations, $\{\mathbf{X}_j\}_{j=1}^J$ are the scatterer locations, $g_r(\mathbf{r})$ are the receiver Green function column vectors, $g_t(\mathbf{r})$ are the transmitter (source) Green function column vectors, τ_j are the scattering amplitudes, and σ_j are the singular values.

The results, presented in Figure 7, show we require an SNR of at least 70 dB to identify all four of the scatterers. Observe how the scatterer singular value magnitudes are very robust against noise. This is a characteristic of the MUSIC algorithm and shows we can monotonically size the scatterers using the singular value magnitude independently of noise.

Example time series for these simulations are presented in Appendix D.

4 Analysis of Scattering Amplitude & SNR

The Foldy-Lax scattering model requires a scattering amplitude, τ, be assigned to each of the point scatterers. Mathematical convergence of the model imposes a maximum bound on the amplitudes. In our model, we set the scattering amplitude of the largest ($\rho_5 = 5$mm) inclusion to

$$\tau_5 \equiv \frac{2\pi}{k_{\max}^2}, \tag{6}$$

and scale the remaining scatterers according to volume:

$$\tau_n = \left(\frac{\rho_n}{\rho_5}\right)^3 \tau_5, \tag{7}$$

for $n = \{3, 1, 0.5\}$mm. Transient scattered responses are modeled by Fourier synthesis. $k_{\max} \equiv 2\pi f_{\max}/v_0$ is the largest wavenumber included in the simulation. The values of the scattering amplitudes are listed in Table 1. The amplitude of the smallest scatterer is shown to be 60 dB down from the largest. We conclude, we require an improvement of at least this much in signal-to-noise ratio (SNR) to be able to measure and detect the response of the smallest scatterer after the largest has been measured and detected. The SNR simulations presented in Figure 7 confirm this. The largest scatterer requires a minimum SNR of 10 dB; the smallest is detected at 70 dB, requiring an improvement of 60 dB.

The pseudospectra results are shown in Appendix E for both operating modes. For each SNR case, we present three figures:

- The pseudospectrum for the top-mounted array;
- The pseudospectrum for the bottom-mounted array;
- The product of the two pseudospectra.

Taking the product of the two pseudospectra improves detectability.

We now compare backscattered amplitudes with respect to the back wall. The amplitude of the field scattered from the back wall located at $z = L$ is approximately

$$A_w \approx \frac{1}{2L}. \tag{8}$$

ρ_n	τ_n	$20\log_{10}(\tau_n/\tau_5)$
5 mm	1.99×10^{-7}	0
3 mm	$0.216\tau_5$	-13 dB
1 mm	$0.008\tau_5$	-42 dB
0.5 mm	$0.001\tau_5$	-60 dB

Table 1: *Scattering amplitudes.*

ρ_n	A_n	$20\log_{10}(A_n/A_w)$
Wall	1.17×10^{-3}	0
5 mm	7.38×10^{-10}	-124 dB
3 mm	1.59×10^{-10}	-137 dB
1 mm	5.91×10^{-12}	-166 dB
0.5 mm	7.38×10^{-13}	-184 dB

Table 2: *Scattered field amplitudes.*

The amplitudes of the scattered fields are approximately

$$A_n \quad \approx \quad \frac{\tau_n}{2z_n}, \tag{9}$$

where z_n is the depth of the scatterer (135 mm). Table 2 lists the gains required to detect the scattered field once the back wall reflection has been detected.

5 Conclusions

We have successfully demonstrated the ability to localize features in a fused silica NIF optic using an ultrasonic time-reversal processing algorithm combined with a MUSIC algorithm for generating detection maps. The algorithm was able to detect, localize, and successfully resolve 3 mm and 5 mm machined hemispherical pits. Our current 1 MHz contiguous transducer array in a single housing provides insufficient signal-to-noise ratio (SNR) to detect the 1 mm and 0.5 mm features. We concluded from simulated SNR tests that a minimum SNR of 70 dB is required to detect all pits. Future arrays used for tomographic purposes must have reduced system noise and low cross-talk between transducer elements. We suggest an array with individually housed elements.

A Forward Field Propagation & Scattering Model

We develop the forward propagation and scattering model which serves as the basis for the time-reversal algorithm. We begin by considering the wave equation

$$\left[\nabla^2 - \frac{n^2(\mathbf{r})}{c_0^2}\partial_t^2\right]\psi^{tot}(\mathbf{r},\mathbf{R}_n^t,t) \quad = \quad -p(\mathbf{r},\mathbf{R}_n^t,t), \tag{10}$$

where we have assumed a variable background through the *refractive index*

$$n(\mathbf{r}) \quad \equiv \quad \frac{c_0}{c(\mathbf{r})}, \tag{11}$$

t is the time variable[1], and $\mathbf{R}_n^t$ is the spatial location of the n-th transmitter. We Fourier transform temporally Eqn. 10 using the transform of Appendix C:

$$\left[\nabla^2 + k_0^2 n^2(\mathbf{r})\right]\psi^{tot}(\mathbf{r},\mathbf{R}_n^t,\omega) \quad = \quad -p(\mathbf{r},\mathbf{R}_n^t,\omega), \tag{12}$$

[1]The appearance of t in a functional argument list indicates the equation or function is taken to be in the time domain. An ω in the same position, indicates the function is in the temporal frequency domain.

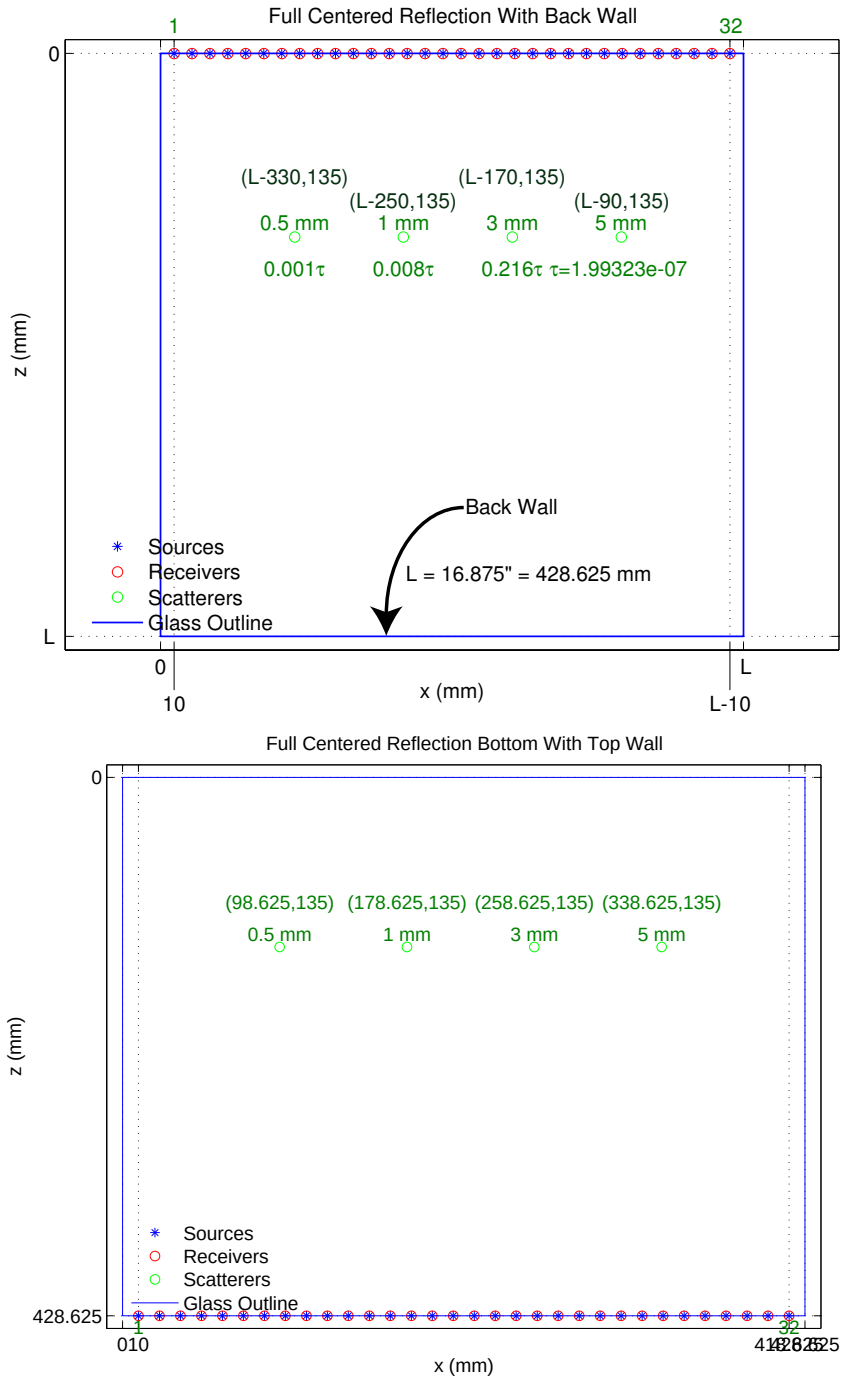

Figure 6: *Full centered reflection geometry from two views: one from the top; one from the bottom. The simulation included reflection from the opposing wall. For this SNR study, we considered 32 multistatic reflection mode transceivers equally distributed over one side of the crystal. The scattering amplitudes used in the simulations are shown below the scatterers. They were set to be directly proportional to the scattering volume. Refer to Section 4 and Appendix B for the details on how they were defined and set.*

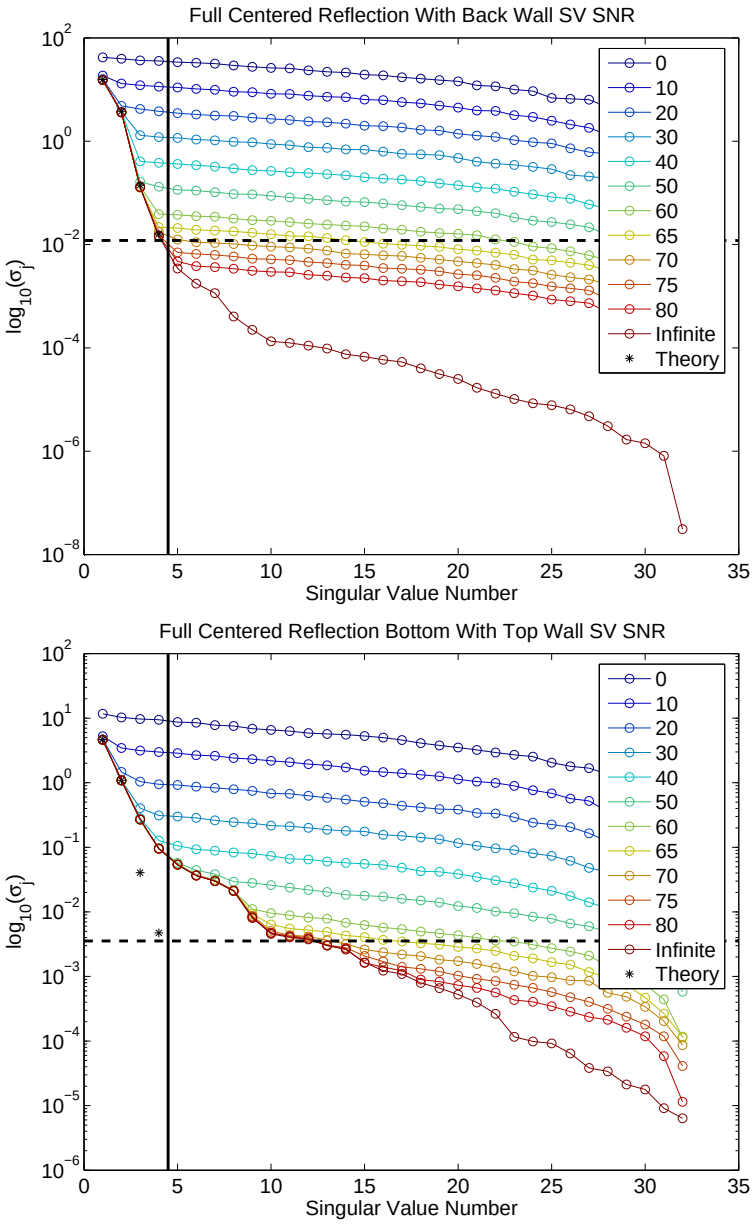

Figure 7: *Singular value SNR results for the full centered reflection geometries with a reflecting wall. We considered SNR values of SNR values of infinity (no noise), and 0 through 80, and compared the results with the theoretical values indicated by the black asterisks. The vertical line delimits the first four singular values corresponding to each of the four scatterers. The dashed horizontal line lies 75% below the smallest scatterer and serves to distinguish between the non-zero and "zero" singular values for the MUSIC algorithm. These results show we require an SNR of at least 70 dB to identify all four scatterers. Observe that the singular value "noise floor" increases as SNR decreases obscuring the smaller scatterers.*

where the *background wavenumber* is defined as

$$k_0 \equiv \frac{\omega}{c_0}.$$

When solving the forward problem, it is frequently convenient to cast Eqn. 12 into an integral equation. We do so by adding $k_0\psi^{tot}(\mathbf{r},\mathbf{R}_n^t,\omega)$ to both sides of Eqn. 12, and moving the inhomogeneous term to the right hand side:

$$\left[\nabla^2 + k_0^2(\omega)\right]\psi^{tot}(\mathbf{r},\mathbf{R}_n^t,\omega) = -p(\mathbf{r}) - \left[k_0^2 n^2(\mathbf{r}) - k_0^2\right]\psi^{tot}(\mathbf{r},\mathbf{R}_n^t,\omega). \tag{13}$$

Define the *object function* as

$$o(\mathbf{r}) \equiv n^2(\mathbf{r}) - 1, \tag{14}$$

and express Eqn. 13 as

$$\left[\nabla^2 + k_0^2(\omega)\right]\psi^{tot}(\mathbf{r},\mathbf{R}_n^t,\omega) = -p(\mathbf{r},\mathbf{R}_n^t,\omega) - k_0^2 o(\mathbf{r})\psi^{tot}(\mathbf{r},\mathbf{R}_n^t,\omega). \tag{15}$$

The first term on the right-hand side of Eqn. 15, $p(\mathbf{r},\mathbf{R}_n^t,\omega)$, is the *primary source* applied to the n-th transmitter. The second, source-like, term on the right-hand side, $k_0^2 o(\mathbf{r})\psi^{tot}(\mathbf{r},\mathbf{R}_n^t,\omega)$, is known as the *secondary source*. We may use Green's theorem to cast the differential equation of Eqn. 15 into an integral equation [13],

$$\begin{aligned}\psi^{tot}(\mathbf{r},\mathbf{R}_n^t,\omega) &= \int d\mathbf{r}'\, G_0(\mathbf{r},\mathbf{r}',\omega)\, p(\mathbf{r}',\mathbf{R}_n^t,\omega) + \\ &\quad k_0^2(\omega)\int d\mathbf{r}'\, G_0(\mathbf{r},\mathbf{r}',\omega)\, o(\mathbf{r}')\, \psi^{tot}(\mathbf{r}',\mathbf{R}_n^t,\omega).\end{aligned} \tag{16}$$

We define the *primary*, *incident*, or *background* field as

$$\psi^{inc}(\mathbf{r},\mathbf{R}_n^t,\omega) \equiv \int d\mathbf{r}'\, G_0(\mathbf{r},\mathbf{r}',\omega)\, p(\mathbf{r}',\mathbf{R}_n^t,\omega), \tag{17}$$

so that Eqn. 16 reads

$$\psi^{tot}(\mathbf{r},\mathbf{R}_n^t,\omega) = \psi^{inc}(\mathbf{r},\mathbf{R}_n^t,\omega) + k_0^2(\omega)\int d\mathbf{r}'\, G_0(\mathbf{r},\mathbf{r}',\omega)\, o(\mathbf{r}')\, \psi^{tot}(\mathbf{r}',\mathbf{R}_n^t,\omega). \tag{18}$$

The *scattered field* is then defined as

$$\begin{aligned}\psi^{scat}(\mathbf{r},\mathbf{R}_n^t,\omega) &\equiv \psi^{tot}(\mathbf{r},\mathbf{R}_n^t,\omega) - \psi^{inc}(\mathbf{r},\mathbf{R}_n^t,\omega) \\ &= k_0^2(\omega)\int d\mathbf{r}'\, G_0(\mathbf{r},\mathbf{r}',\omega)\, o(\mathbf{r}')\, \psi^{tot}(\mathbf{r}',\mathbf{R}_n^t,\omega).\end{aligned} \tag{19}$$

We observe that with the primary field satisfying

$$\left[\nabla^2 + k_0^2(\omega)\right]\psi^{inc}(\mathbf{r},\mathbf{R}_n^t,\omega) = -p(\mathbf{r},\mathbf{R}_n^t,\omega), \tag{20}$$

the scattered field obeys

$$\left[\nabla^2 + k_0^2\right]\psi^{scat}(\mathbf{r},\mathbf{R}_n^t,\omega) = -k_0^2 o(\mathbf{r})\psi^{tot}(\mathbf{r},\mathbf{R}_n^t,\omega), \tag{21}$$

or alternatively,

$$\left[\nabla^2 + k_0^2 n^2(\mathbf{r})\right]\psi^{scat}(\mathbf{r},\mathbf{R}_n^t,\omega) = -k_0^2 o(\mathbf{r})\psi^{inc}(\mathbf{r},\mathbf{R}_n^t,\omega). \tag{22}$$

A.1 Born Approximation

One potential method of simplifying Eqn. 22 for solving is to use a perturbation method approach. We express the express the refractive index and scattered field as [14]

$$\begin{aligned} n^2(\mathbf{r}) &= n_0^2(\mathbf{r}) + \underbrace{\epsilon n_1(\mathbf{r}) + \epsilon^2 n_2(\mathbf{r}) + \cdots}_{\equiv\, \delta n(\mathbf{r})}, \\ \psi^{scat}(\mathbf{r}, \mathbf{R}_n^t, \omega) &= \psi_{DWB}^{scat}(\mathbf{r}, \mathbf{R}_n^t, \omega) + \epsilon \psi_1^{scat}(\mathbf{r}, \mathbf{R}_n^t, \omega) + \epsilon^2 \psi_2^{scat}(\mathbf{r}, \mathbf{R}_n^t, \omega) + \cdots, \end{aligned} \tag{23}$$

respectively, substitute them into Eqn. 22, and equating like powers of ϵ. Doing so we obtain the follow set of equations:

$$\left[\nabla^2 + k_0^2 n_0^2(\mathbf{r})\right] \psi_{DWB}^{scat}(\mathbf{r}, \mathbf{R}_n^t, \omega) = -k_0^2 o(\mathbf{r}) \psi^{inc}(\mathbf{r}, \mathbf{R}_n^t, \omega), \tag{24}$$

$$\left[\nabla^2 + k_0^2 n_0^2(\mathbf{r})\right] \psi_1^{scat}(\mathbf{r}, \mathbf{R}_n^t, \omega) = -k_0^2 n_1(\mathbf{r}) \psi_{DWB}^{scat}(\mathbf{r}, \mathbf{R}_n^t, \omega), \tag{25}$$

$$\left[\nabla^2 + k_0^2 n_0^2(\mathbf{r})\right] \psi_2^{scat}(\mathbf{r}, \mathbf{R}_n^t, \omega) = -k_0^2 n_2(\mathbf{r}) \psi_{DWB}^{scat}(\mathbf{r}, \mathbf{R}_n^t, \omega) - k_0^2 n_1(\mathbf{r}) \psi_1^{scat}(\mathbf{r}, \mathbf{R}_n^t, \omega), \tag{26}$$

$$\vdots$$

$$\left[\nabla^2 + k_0^2 n_0^2(\mathbf{r})\right] \psi_l^{scat}(\mathbf{r}, \mathbf{R}_n^t, \omega) = -k_0^2 \sum_{m=0}^{l-1} n_{l-m}(\mathbf{r}) \psi_m^{scat}(\mathbf{r}, \mathbf{R}_n^t, \omega). \tag{27}$$

The Green function for the left hand side operators of Eqns 24 through 26 satisfies

$$\left[\nabla^2 + k_0^2 n_0^2(\mathbf{r})\right] G(\mathbf{r}, \mathbf{r}', \omega) = -\delta(\mathbf{r} - \mathbf{r}'). \tag{28}$$

Using this to cast Eqn. 24 into an integral equation, we obtain the *distorted wave Born approximation* to the scattered field,

$$\psi_{DWB}^{scat}(\mathbf{r}, \mathbf{R}_n^t, \omega) = k_0^2 \int d\mathbf{r}'\, G(\mathbf{r}, \mathbf{r}', \omega)\, o(\mathbf{r}')\, \psi^{inc}(\mathbf{r}', \mathbf{R}_n^t, \omega). \tag{29}$$

When $n_0(\mathbf{r}) \equiv 1$, this reduces to the standard *Born approximation* [15],

$$\psi_B^{scat}(\mathbf{r}, \mathbf{R}_n^t, \omega) = k_0^2 \int d\mathbf{r}'\, G_0(\mathbf{r}, \mathbf{r}', \omega)\, o(\mathbf{r}')\, \psi^{inc}(\mathbf{r}', \mathbf{R}_n^t, \omega). \tag{30}$$

In free space we have

$$G_0(\mathbf{r}, \mathbf{r}', \omega) \equiv \frac{1}{4\pi\, |\mathbf{r} - \mathbf{r}'|}\, e^{ik_0 |\mathbf{r} - \mathbf{r}'|} \tag{31}$$

A.2 Incident Field

The incident field is taken to be a spherical wave due to a point source located at $\mathbf{R}_n^t$. We express this mathematically as

$$\psi^{inc}(\mathbf{r}) = P(\omega)\, G_0(\mathbf{r}, \mathbf{R}_n^t, \omega), \tag{32}$$

where $P(\omega)$ is the temporal spectrum of the incident field, and $G_0(\mathbf{r}, \mathbf{r}', \omega)$ is the Green function response of the medium. We then express Eqn. 30 as

$$\psi_B^{scat}(\mathbf{r}, \mathbf{R}_n^t, \omega) = k_0^2\, P(\omega) \int d\mathbf{r}'\, G_0(\mathbf{r}, \mathbf{r}', \omega)\, o(\mathbf{r}')\, G_0(\mathbf{r}', \mathbf{R}_n^t, \omega). \tag{33}$$

This is our forward scattering model for the time-reversal scattering target detection described in the next section.

B Time-Reversal

Mathematically, time-reversal (TR) falls into a category of imaging and detection techniques based upon decomposition of either the measured data, the scattering operator, or the object to be imaged. TR decomposes the measured data via a singular value decomposition [3, 2]. We explain as follows. Define the *receiver* and *transmitter* Green function column vectors as follows

$$g_r(\mathbf{r}) \equiv [G_0(\mathbf{R}_1^r, \mathbf{r}),\ G_0(\mathbf{R}_2^r, \mathbf{r}),\ \cdots, G_0(\mathbf{R}_M^r, \mathbf{r})]^T, \tag{34}$$

$$g_t(\mathbf{r}) \equiv P(\omega)\left[G_0(\mathbf{r}, \mathbf{R}_1^t),\ G_0(\mathbf{r}, \mathbf{R}_2^t),\ \cdots,\ G_0(\mathbf{r}, \mathbf{R}_N^t)\right]^T, \tag{35}$$

where there are M receivers, N transmitters, $\{\mathbf{R}_m^r\}_{m=1}^M$ are the receiver locations, $\{\mathbf{R}_n^t\}_{n=1}^N$ are the transmitter locations, and for notational compactness, we have omitted the ω dependence.

Using these definitions, the forward model of Eqn. 33 represents the integral of the object function with the outer product of the Green function vectors:

$$D(\omega) = k_0^2(\omega) \int d\mathbf{r}\ g_r(\mathbf{r})\ o(\mathbf{r})\ g_t^T(\mathbf{r}), \tag{36}$$

where $D(\omega)$ is the $M \times N$ of measured scattered field values, $\psi_B^{scat}(\mathbf{R}_m^r, \mathbf{R}_n^t, \omega)$.

In the general case where all of the transmitters are simultaneously activated, and the data measured at all the receivers, we may represent the forward scattering process by a matrix multiplication of the form

$$v = Ke$$

where $v = v(\omega)$ is the linear array of output values, viewed as an M dimensional column vector, measured at the receivers, $e = e(\omega)$ is the N dimensional column vector of applied excitations to the transmitters, K is the $M \times N$ multistatic matrix. We will not explicitly display the frequency variable ω in subsequent equations. In time-reversal imaging the object profile $o(\mathbf{r})$ consists of a sum of $J \leq \min(N, M)$ disjoint profiles $o_j(\mathbf{r})$ each centered at a spatial location $\mathbf{X}_j$ and each having an effective size that is small relative to the wavelength; i.e.,

$$o(\mathbf{r}) = \sum_{j=1}^J o_j(\mathbf{r} - \mathbf{X}_j) = \sum_{j=1}^J \tau_j\ \delta(\mathbf{r} - \mathbf{X}_j). \tag{37}$$

The goal of time-reversal imaging is then to estimate the location $\mathbf{X}_j$ and strength of each scatterer. If we substitute Eqn. 37 into Eqn. 36 we obtain

$$K = k_0^2(\omega) \sum_{j=1}^J \int d\mathbf{r}\ g_r(\mathbf{r})\ o_j(\mathbf{r} - \mathbf{X}_j)\ g_t^T(\mathbf{r}) = k_0^2(\omega) \sum_{j=1}^J \tau_j\ g_r(\mathbf{X}_j)\ g_t^T(\mathbf{X}_j) \tag{38}$$

where

$$\tau_j = \int d\mathbf{r}\ o_j(\mathbf{r}) \tag{39}$$

and where we have made use of the assumption that the targets are small relative to the wavelength. The quantities τ_j thus represent effective *reflection coefficients* for the targets and the goal of time-reversal imaging is then to estimate these reflection coefficients as well as the target locations $\mathbf{X}_j$.

B.1 Singular Value Decomposition of the Multi-Static Matrix

The theory of time-reversal imaging depends on the ability to perform a singular value decomposition (SVD) of the multistatic data matrix K. In particular, we consider the singular system

$$K: \quad C^N \to C^M \qquad Ke_i = \sigma_i v_i, \tag{40}$$

$$K^\dagger: \quad C^M \to C^N \qquad K^\dagger v_i = \sigma_i e_i, \tag{41}$$

where i labels the singular system e_i, v_i, σ_i. The normal equations for this system are

$$K^\dagger K e_i = \sigma_i^2 e_i, \tag{42}$$
$$K K^\dagger v_i = \sigma_i^2 v_i, \tag{43}$$

where the $N \times N$ matrix

$$T = K^\dagger K, \tag{44}$$

$$\overbrace{T_1 = K^\dagger K}^{\text{Transmitter to Receiver}} \qquad \overbrace{T_2 = K K^\dagger}^{\text{Receiver to Transmitter}}$$

is the well-known *time-reversal matrix*. The singular vectors $\{e_i\}_{i=1}^N$ are orthonormal and span the space C^N while the singular vectors $\{v_i\}_{i=1}^M$ are orthonormal and span the space C^M. There are a total of min (N, M) singular values $\sigma_j \geq 0$.

If we substitute the expression for the K matrix given in Eqn. 38) into Eqns. 40 and 41 we obtain

$$k_0^2(\omega) \sum_{j=1}^{J} \tau_j g_r(\mathbf{X}_j) g_t^T(\mathbf{X}_j) e_i = \sigma_i v_i \tag{45}$$

$$k_0^2(\omega) \sum_{j=1}^{J} \tau_j^* g_t^*(\mathbf{X}_j) g_r^\dagger(\mathbf{X}_j) v_i = \sigma_i e_i \tag{46}$$

It follows from the above equations that the singular vectors v_i are linear combinations of the receiver array Green function vectors $g_r(\mathbf{X}_j)$ while the singular vectors e_i are linear combinations of the complex conjugates of the transmitter array Green function vectors $g_t^*(\mathbf{X}_j)$. An important special case occurs when these two sets of Green function vectors are orthogonal; i.e., when the following two equations are satisfied:

$$g_r^\dagger(\mathbf{X}_j) g_r(\mathbf{X}_{j'}) = \|g_r(\mathbf{X}_j)\|^2 \delta_{j,j'} = H_r(\mathbf{X}_j, \mathbf{X}_{j'}) \tag{47}$$
$$g_t^\dagger(\mathbf{X}_j) g_t(\mathbf{X}_{j'}) = \|g_t(\mathbf{X}_j)\|^2 \delta_{j,j'} = H_t(\mathbf{X}_j, \mathbf{X}_{j'}) \tag{48}$$

where $\delta_{j,j'}$ is the Kronecker delta function and

$$||g_r(\mathbf{X}_j)||^2 = g_r^\dagger(\mathbf{X}_j) g_r(\mathbf{X}_j)$$
$$||g_r(\mathbf{X}_j)||^2 = g_r^\dagger(\mathbf{X}_j) g_r(\mathbf{X}_j)$$

are the squared norms of the Green function vectors evaluated at the target point $\mathbf{X}_j$. If Eqn. 47 holds then we say that *the targets are well resolved by the receiver array* while if Eqn. 48 holds we say that *the targets are well resolved by the transmitter array*. When both equations hold then the targets are well resolved with respect to both the transmitter and receiver arrays.

The rational for the above terminology is apparent if we simply note that the inner products in Eqns. 47 and 48 are, respectively, the PSF's $H_r(\mathbf{X}_j, \mathbf{X}_{m'})$ and $H_t(\mathbf{X}_j, \mathbf{X}_{m'})$. Thus, for example, the inner product $g_r^\dagger(\mathbf{X}_j) g_r(\mathbf{X}_{j'})$ is *the image of a point target located at $\mathbf{X}_{j'}$ formed at point $\mathbf{X}_j$ by the receiver array*. An entirely analogous interpretation can be given the inner product $g_t^\dagger(\mathbf{X}_j) g_t(\mathbf{X}_{j'})$; i.e., as *the image of a point target located at $\mathbf{X}_{j'}$ formed at point $\mathbf{X}_j$ by the transmitter array.* The case of *well resolved targets* thus corresponds to the case where the targets are sufficiently well separated that the PSF of either the transmitter or receiver array does not significantly overlap any target other than the one on which it is focused.

B.2 Well-resolved Targets

We will assume hence forth that the targets are well resolved with respect to both the transmitter and receiver arrays, and that both Eqns. 47 and 48 hold. In this case it is easy to show that *the singular system $\{e_i, v_i, \sigma_i > 0\}$ can be related in a one-to-one manner with the $J \leq$ min(N, M) scattering targets*. Indeed, it follows at once from the

Transmitter C^N Space	**Receiver C^M Space**
Let $N_\sigma \equiv \min(N, M)$	
$Ke_j = \sigma_j v_j, \quad j = 1, \cdots, J$ $Ke_j = 0, \quad j = J+1, \cdots, N_\sigma$ $e_j^\dagger e_{j'} = \delta_{jj'}$ $\mathcal{S}^t \equiv \text{span}\{e_j,\ j = 1, \cdots, J\}$ $\mathcal{N}^t \equiv \text{span}\{e_j,\ j = J+1, \cdots, N_\sigma\}$ $C^N = \mathcal{S}^t \oplus \mathcal{N}^t$	$K^\dagger v_j = \sigma_j e_j, \quad j = 1, \cdots, J$ $K^\dagger v_j = 0, \quad j = J+1, \cdots, N_\sigma$ $v_j^\dagger v_{j'} = \delta_{jj'}$ $\mathcal{S}^r \equiv \text{span}\{v_j,\ j = 1, \cdots, J\}$ $\mathcal{N}^r \equiv \text{span}\{v_j,\ j = J+1, \cdots, N_\sigma\}$ $C^M = \mathcal{S}^r \oplus \mathcal{N}^r$

Table 3: *Mathematical relations of the transmitter and receiver spaces defined by the transmitter and receiver singular vectors. $\mathcal{S}^t$ and $\mathcal{N}^t$ represent the transmitter signal and noise subspaces, respectively. $\mathcal{S}^r$ and $\mathcal{N}^r$ represent the receiver signal and noise subspaces, respectively.*

orthogonality of the Green function vectors that the singular vectors having non-zero singular values for well-resolved targets are given by

$$e_j = \frac{g_t^*(\mathbf{X}_j)}{||g_t(\mathbf{X}_j)||}, \tag{49}$$

$$v_j = \frac{g_r(\mathbf{X}_j)}{||g_r(\mathbf{X}_j)||} \tag{50}$$

where $j = 1, 2, \ldots, J$. Moreover, the non-zero singular values σ_j are given by

$$\sigma_j = k_0^2(\omega)\ |\tau_j|\ \|g_t(\mathbf{X}_j)\|\ \|g_r(\mathbf{X}_j)\|\,. \tag{51}$$

We conclude that *the scatterer strengths are computed directly from the singular values* which, in turn, are readily computed from the measured multistatic data matrix K. Moreover, *the singular vectors give the location of the targets.* Indeed, the coherent image formed using the singular vector e_j will generate the PSF of the transmitter array centered at $\mathbf{X}_j$ while the coherent image formed using the singular vector v_j will generate the PSF of the receiver array centered at $\mathbf{X}_j$.

B.3 Pseudospectrum

For well resolved targets, the $\{e_n\}_{n=1}^N$, and $\{v_m\}_{m=1}^M$ form two orthonormal sets which span the C^N and C^M spaces, respectively. The transmitter and receiver spaces may be subdivided into *signal* and *noise* subspaces based upon the span of the $\{e_j\}_{j=1}^{J \le \min(N,M)}$ and $\{v_j\}_{j=1}^{J \le \min(N,M)}$ vectors where J is the number of point scatterers. These properties are summarized mathematically in Table 3.

We may use these properties to construct an algorithm to image the scatterers. Consider the transmitter and receiver Green's function vectors, $g_t(\mathbf{r})$ and $g_r(\mathbf{r})$, as defined in Eqn. 34 and Eqn. 35, respectively[2]. When the point at which

[2]We have dropped the explicit dependence upon the temporal frequency, ω, in the notation.

these Green's function vectors falls upon a scatterer location, $\mathbf{X}_j$, we have

$$\left.\begin{array}{rcccl} e_j^T g_t(\mathbf{X}_j) & = & \dfrac{1}{\|g_t(\mathbf{X}_j)\|}\, g_t^\dagger(\mathbf{X}_j) g_t(\mathbf{X}_j) & = & \|g_t(\mathbf{X}_j)\|, \\ v_j^\dagger g_r(\mathbf{X}_j) & = & \dfrac{1}{\|g_r(\mathbf{X}_j)\|}\, g_r^\dagger(\mathbf{X}_j) g_r(\mathbf{X}_j) & = & \|g_r(\mathbf{X}_j)\|, \end{array}\right\} \text{for } j \;=\; 1, \cdots, J, \tag{52}$$

and

$$\left.\begin{array}{rcl} e_{j'}^T g_t(\mathbf{X}_j) & = & 0, \\ v_{j'}^\dagger g_r(\mathbf{X}_j) & = & 0, \end{array}\right\} \text{for } j' \;=\; J+1, \cdots, \min(N, M), \tag{53}$$

where we have used the definitions of the e_j and v_j singular vectors from Eqns. 49 and 50. For other evaluation points, that is, for spatial locations, $\mathbf{r}$, which are not scatterer locations, we have

$$\left.\begin{array}{rcl} e_{j'}^T g_t(\mathbf{r}) & \neq & 0, \\ v_{j'}^\dagger g_r(\mathbf{r}) & \neq & 0, \end{array}\right\} \text{for } j' \;=\; J+1, \cdots, \min(N, M), \text{ and } \mathbf{r} \;\neq\; \mathbf{X}_j. \tag{54}$$

Consider the following sum of the inner products of the singular vectors and transceiver Green's function vectors:

$$Q(\mathbf{r}) \quad \equiv \quad \sum_{j=J+1}^{\min(N,M)} \left[\left| e_j^T g_t(\mathbf{r}) \right| + \left| v_j^\dagger g_r(\mathbf{r}) \right| \right]. \tag{55}$$

When we evaluate Eqn. 55 at any scatterer location, $\mathbf{r} = \mathbf{X}_j$, we have

$$Q(\mathbf{X}_j) \quad \equiv \quad 0, \;\; \text{for } j = 1, \cdots, J,$$

where we have used the orthogonality property of Eqn. 53. We now define the *pseudospectrum* to be

$$P(\mathbf{r}) \quad \equiv \quad \frac{1}{\displaystyle\sum_{j=J+1}^{\min(N,M)} \left[\left| e_j^T g_t(\mathbf{r}) \right| + \left| v_j^\dagger g_r(\mathbf{r}) \right| \right] + \sigma_r}, \tag{56}$$

where σ_r is a regularization parameter. For well resolved scatterers, $P(\mathbf{r})$ will have distinct peaks at each of the scatterer locations. We wish to emphasize that the pseudospectrum is a *detection* map rather than an actual image of the scatterers. By Eqns. 53 and 54, we observe that Eqn. 56 is highly peaked (in fact, it diverges for $\sigma_r \equiv 0$) when $\mathbf{r} \equiv \mathbf{X}_j$.

We note the expression in Eqn. 56 combines the transmitters and receivers into a "super-array" with steering vectors e_j^T applied to the transmitters, and $v_j^\dagger$ applied to the receivers.

C Standard Fourier Transforms

We summarize without comment our Fourier transform definitions.

Forward in time

$$U(\mathbf{r}, \omega) \quad = \quad \int_{-\infty}^{\infty} dt \; u(\mathbf{r}, t) \; e^{i\omega t}$$

Inverse in time

$$u(\mathbf{r},t) \quad = \quad \frac{1}{2\pi}\int_{-\infty}^{\infty} d\omega\, U(\mathbf{r},\omega)\, e^{-i\omega t}$$

Forward in space

$$\tilde{U}(\mathbf{k},\omega) \quad = \quad \int_{-\infty}^{\infty} d\mathbf{r}\, U(\mathbf{r},\omega)\, e^{-i\mathbf{k}\cdot\mathbf{r}}$$

Inverse in space

$$U(\mathbf{r},\omega) \quad = \quad \frac{1}{(2\pi)^3}\int_{-\infty}^{\infty} d\mathbf{k}\, \tilde{U}(\mathbf{k},\omega)\, e^{i\mathbf{k}\cdot\mathbf{r}}$$

D Sample Simulated Scattered Time Series

0 dB

Top Reflection

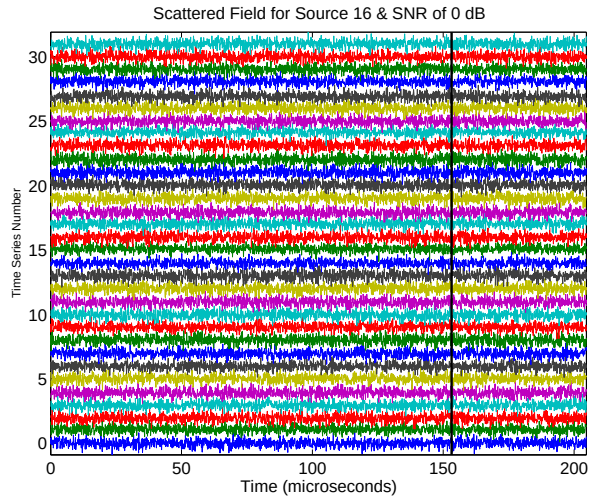

Bottom Reflection

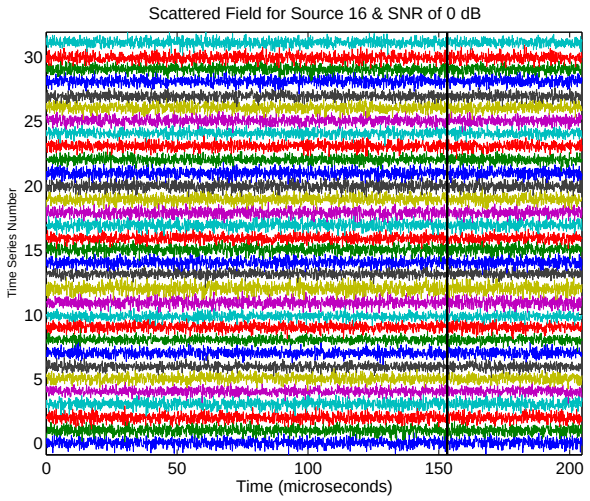

Sample scattered field time series at 0 dB.

10 dB

Top Reflection

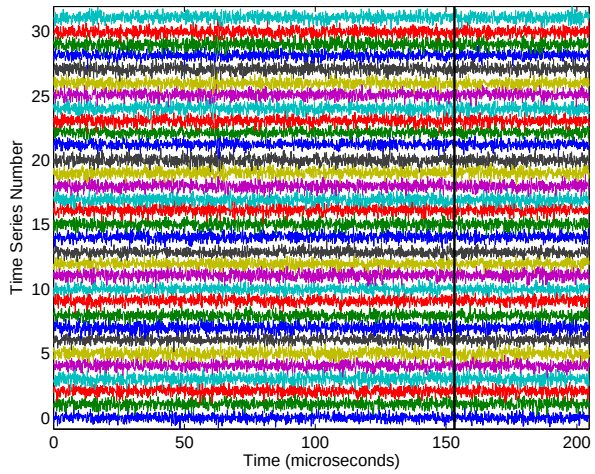

Bottom Reflection

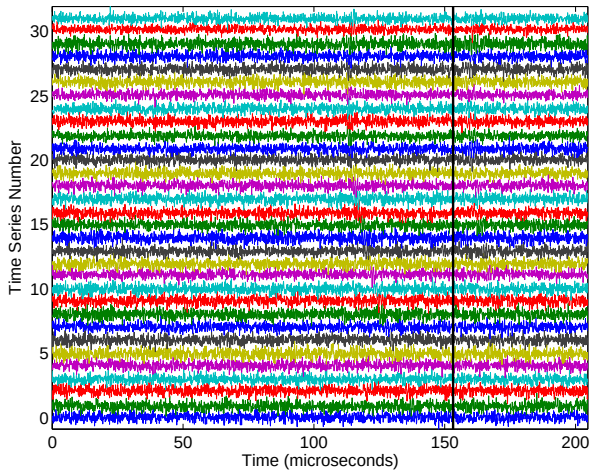

Sample scattered field time series at 10 dB.

20 dB

Top Reflection

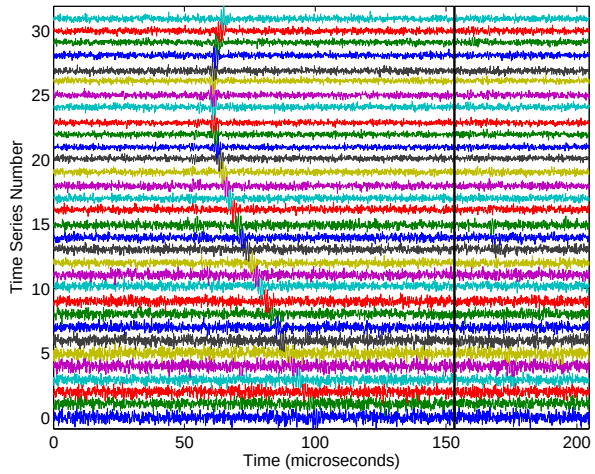

Bottom Reflection

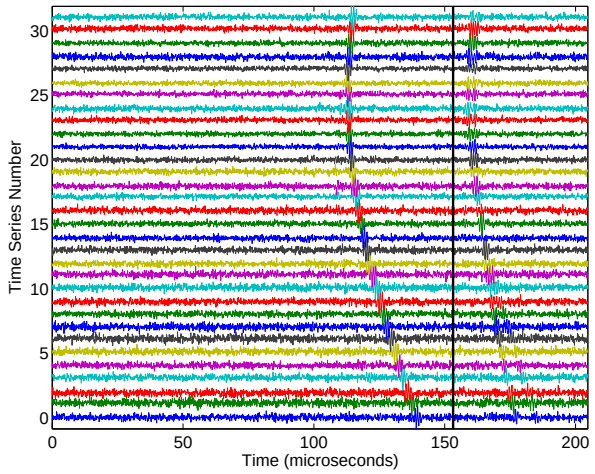

Sample scattered field time series at 20 dB.

30 dB

Top Reflection

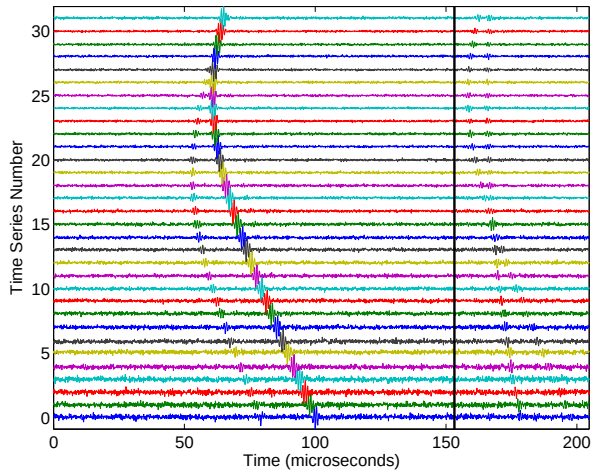

Bottom Reflection

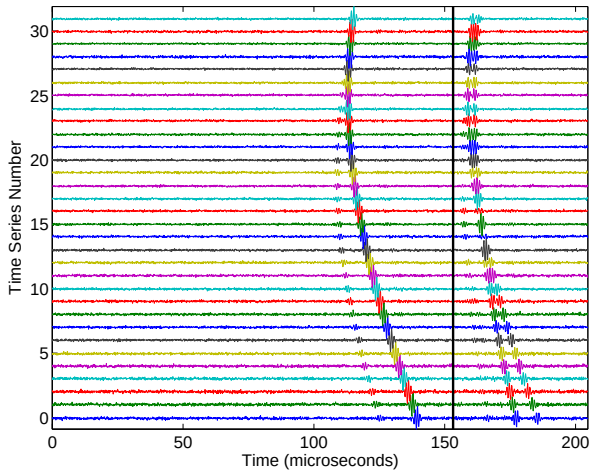

Sample scattered field time series at 30 dB.

40 dB

Top Reflection

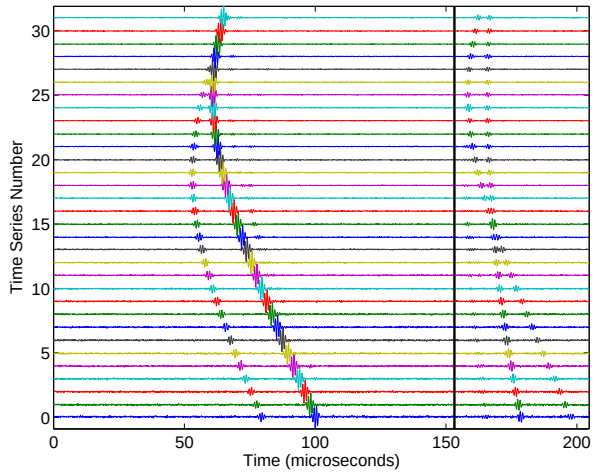

Bottom Reflection

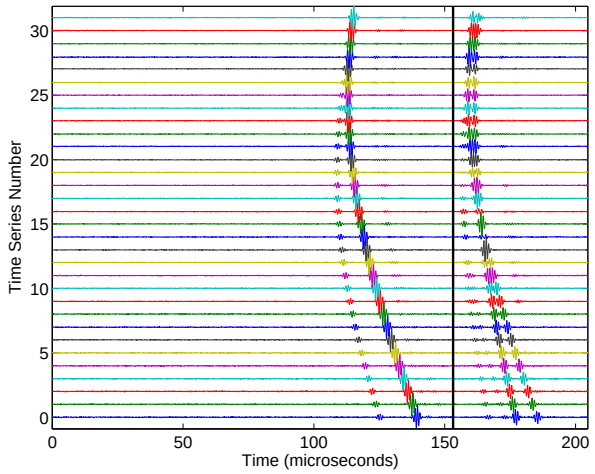

Sample scattered field time series at 40 dB.

50 dB

Top Reflection

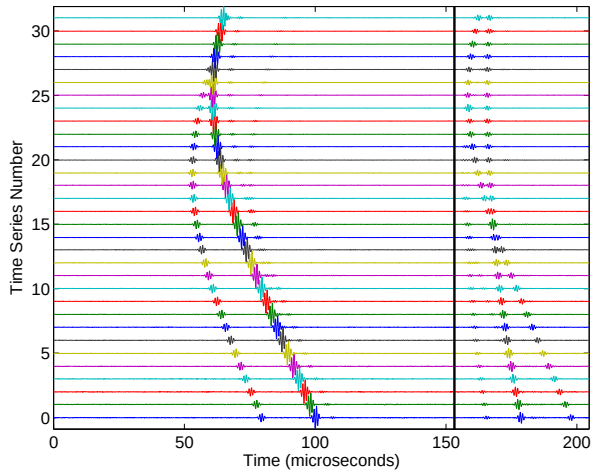

Bottom Reflection

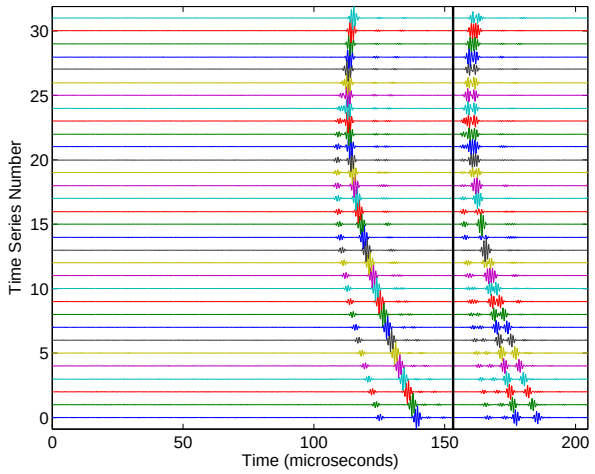

Sample scattered field time series at 50 dB.

60 dB

Top Reflection

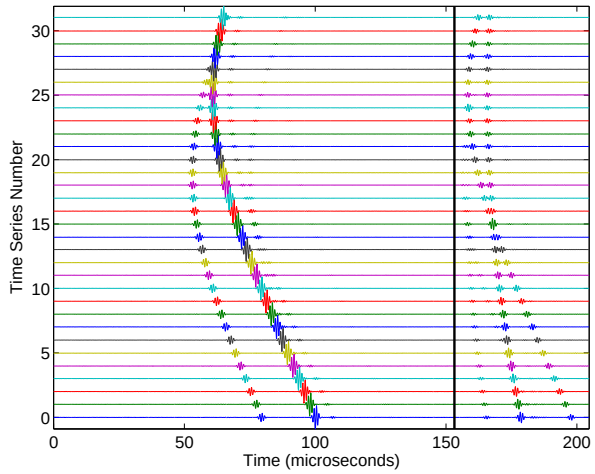

Bottom Reflection

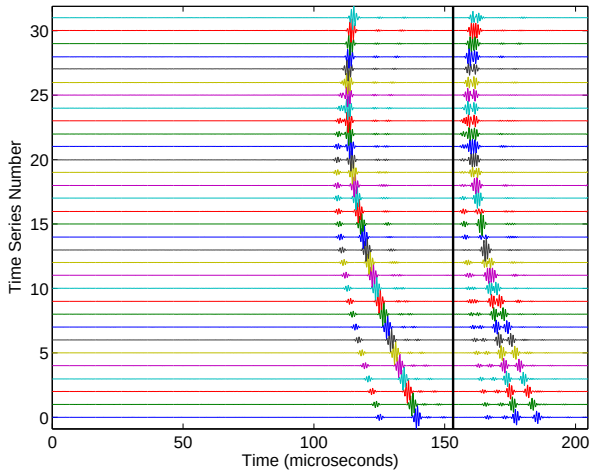

Sample scattered field time series at 60 dB.

65 dB

Top Reflection

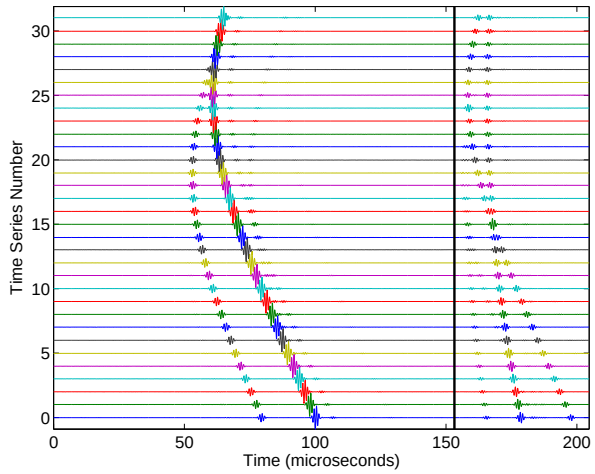

Bottom Reflection

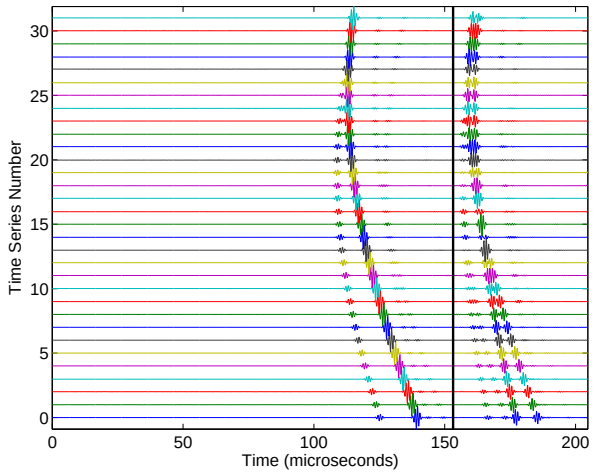

Sample scattered field time series at 65 dB.

70 dB

Top Reflection

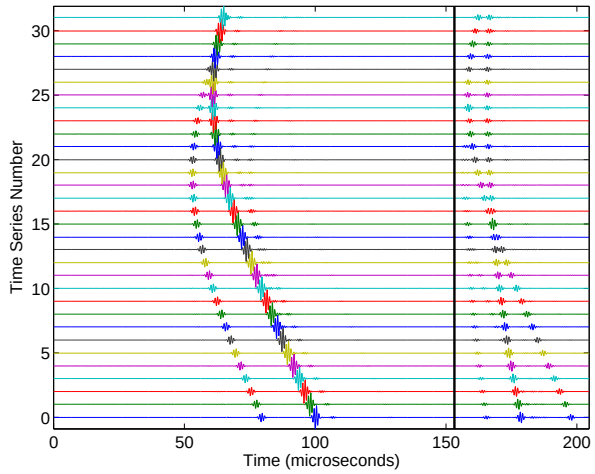

Bottom Reflection

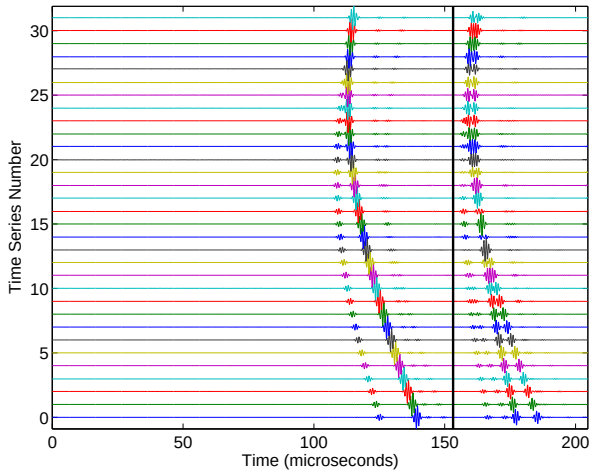

Sample scattered field time series at 70 dB.

75 dB

Top Reflection

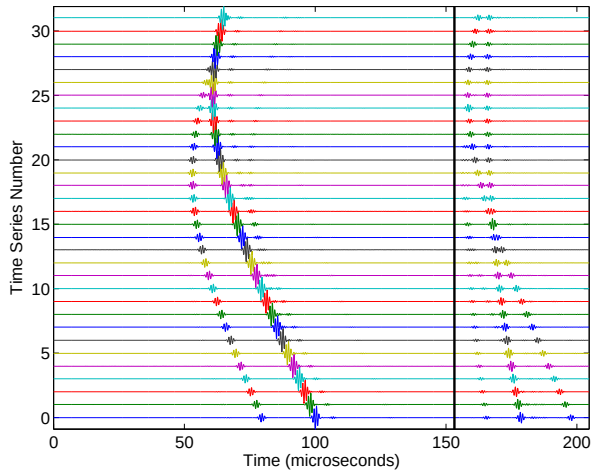

Bottom Reflection

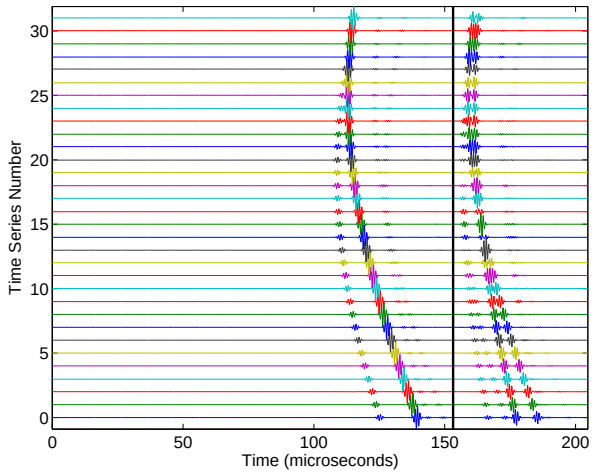

Sample scattered field time series at 75 dB.

80 dB

Top Reflection

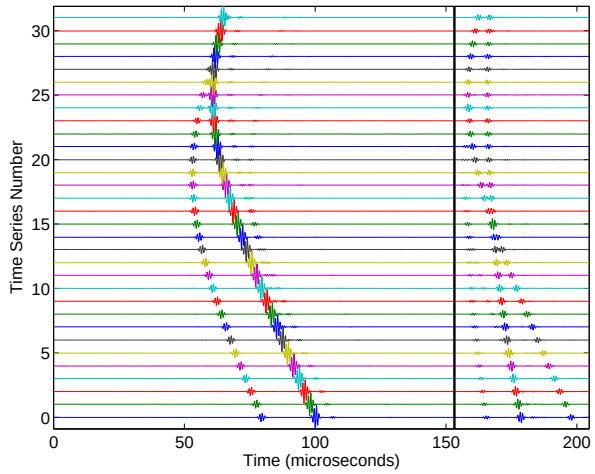

Bottom Reflection

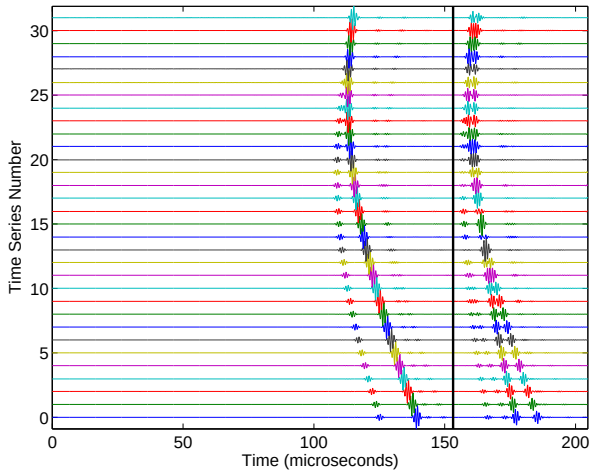

Sample scattered field time series at 80 dB.

∞ dB

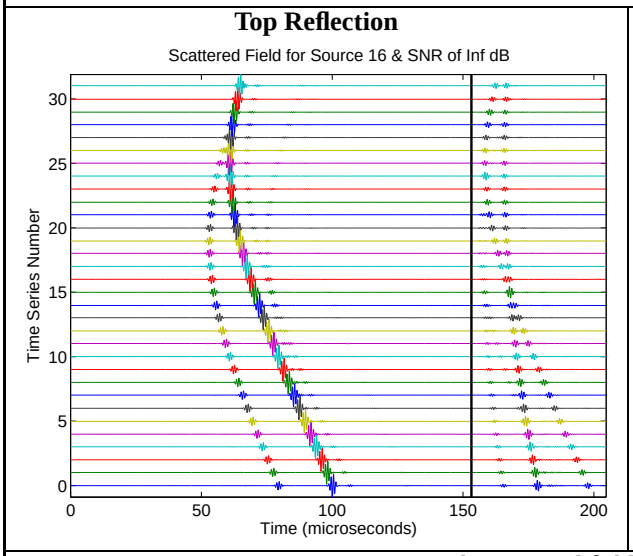

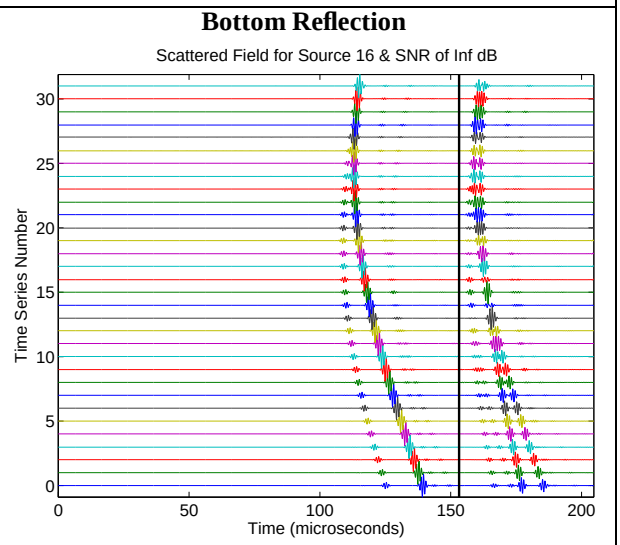

Sample scattered field time series at ∞ dB.

E Pseudospectra Results

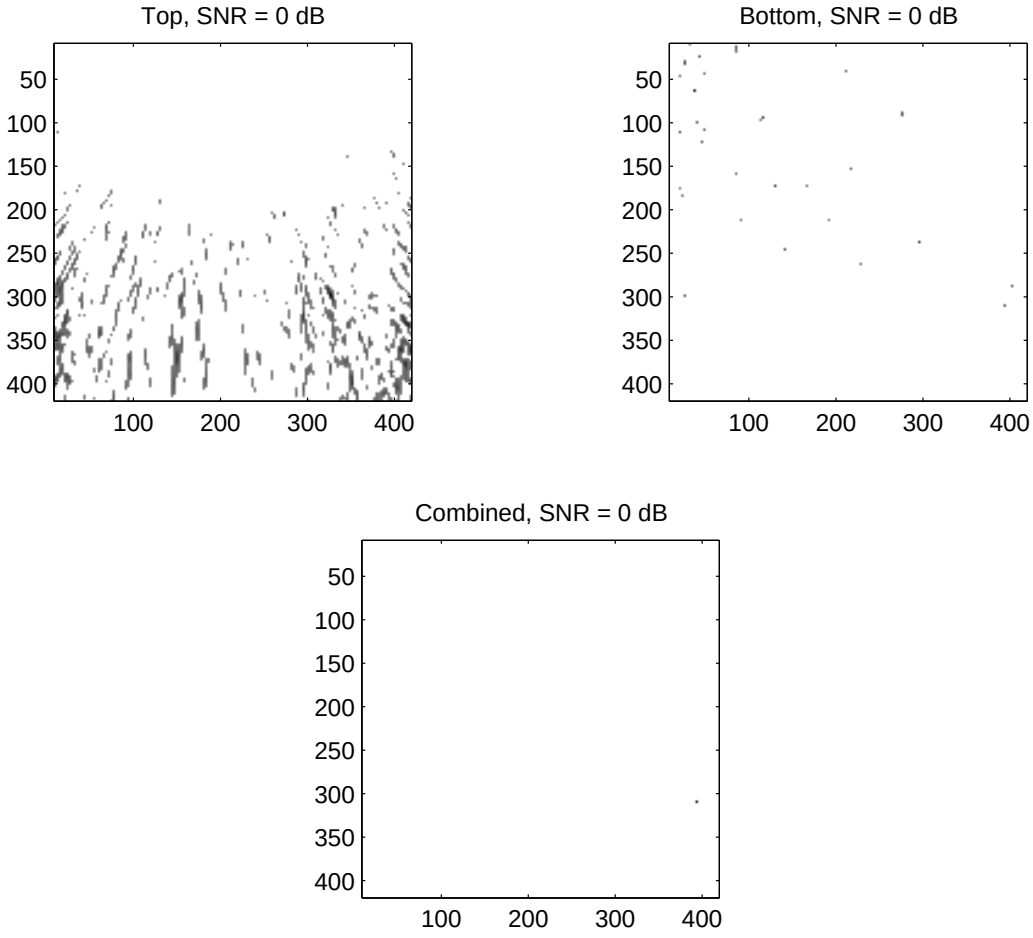

Combined thresholded pseudospectra at an SNR of 0 dB.

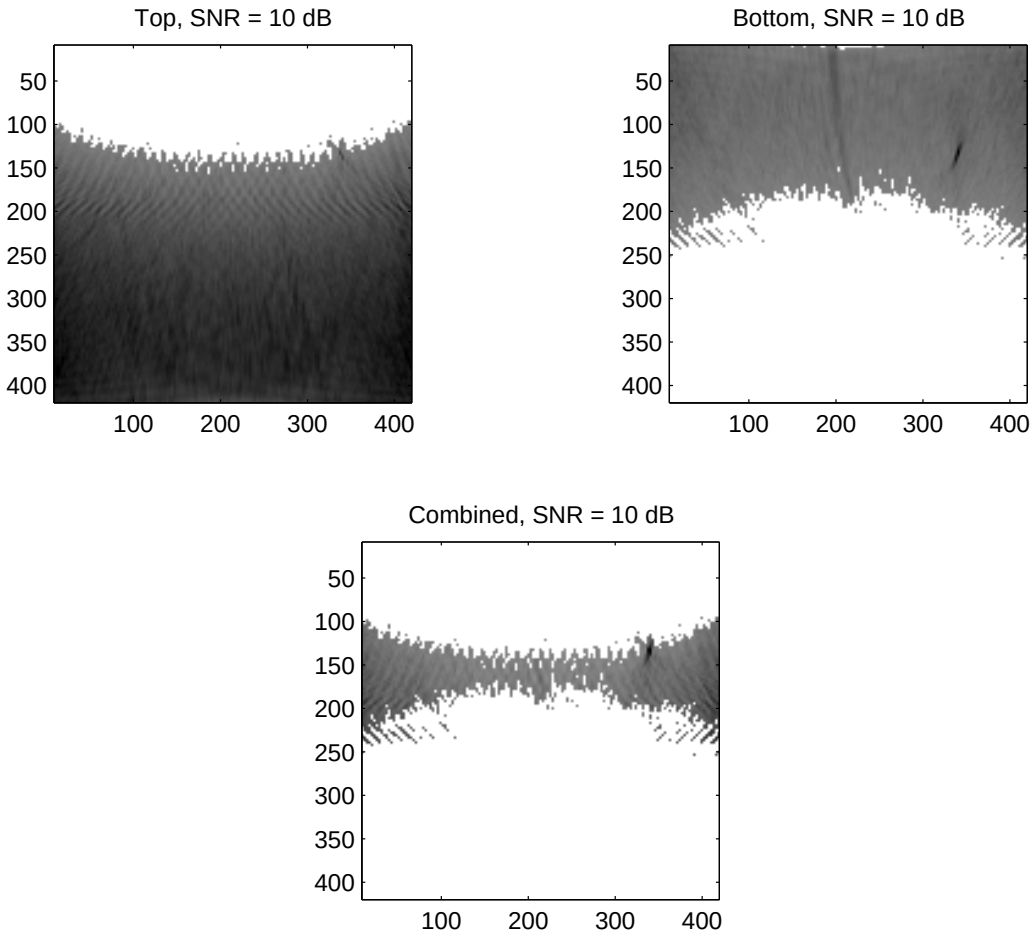

Combined thresholded pseudospectra at an SNR of 10 dB.

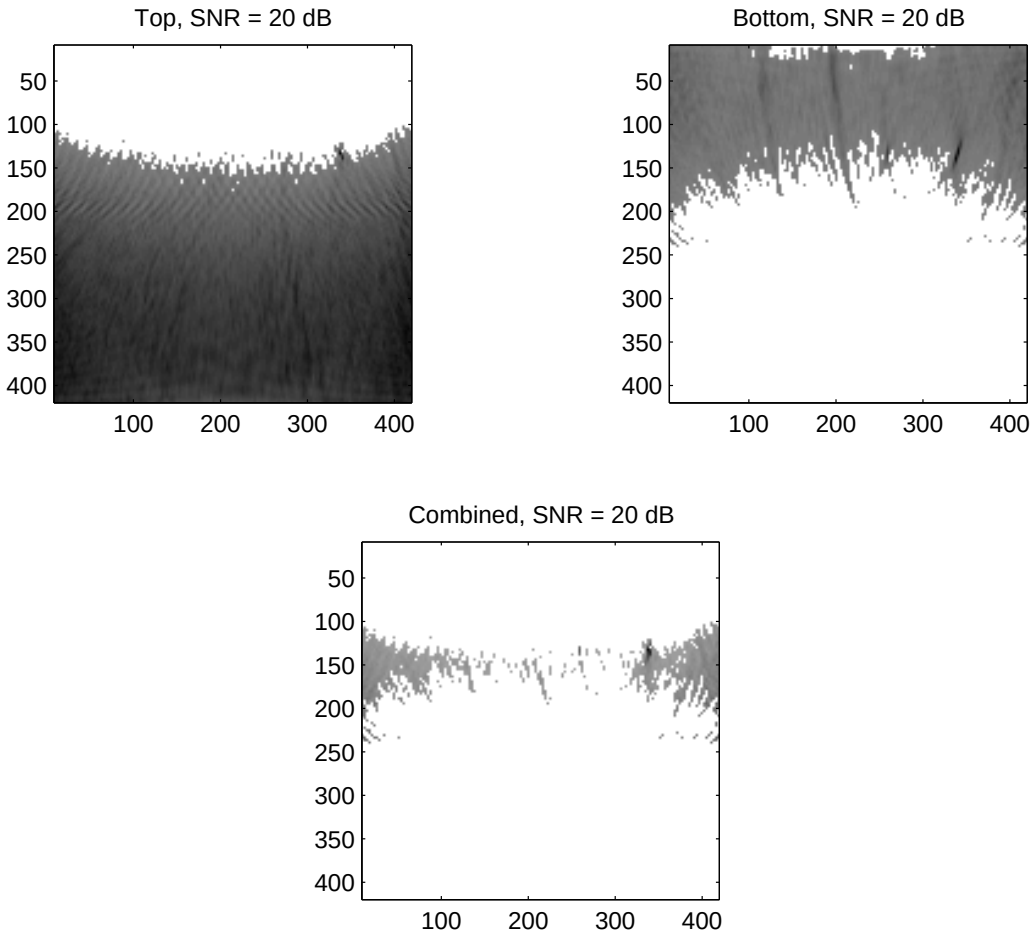

Combined thresholded pseudospectra at an SNR of 20 dB.

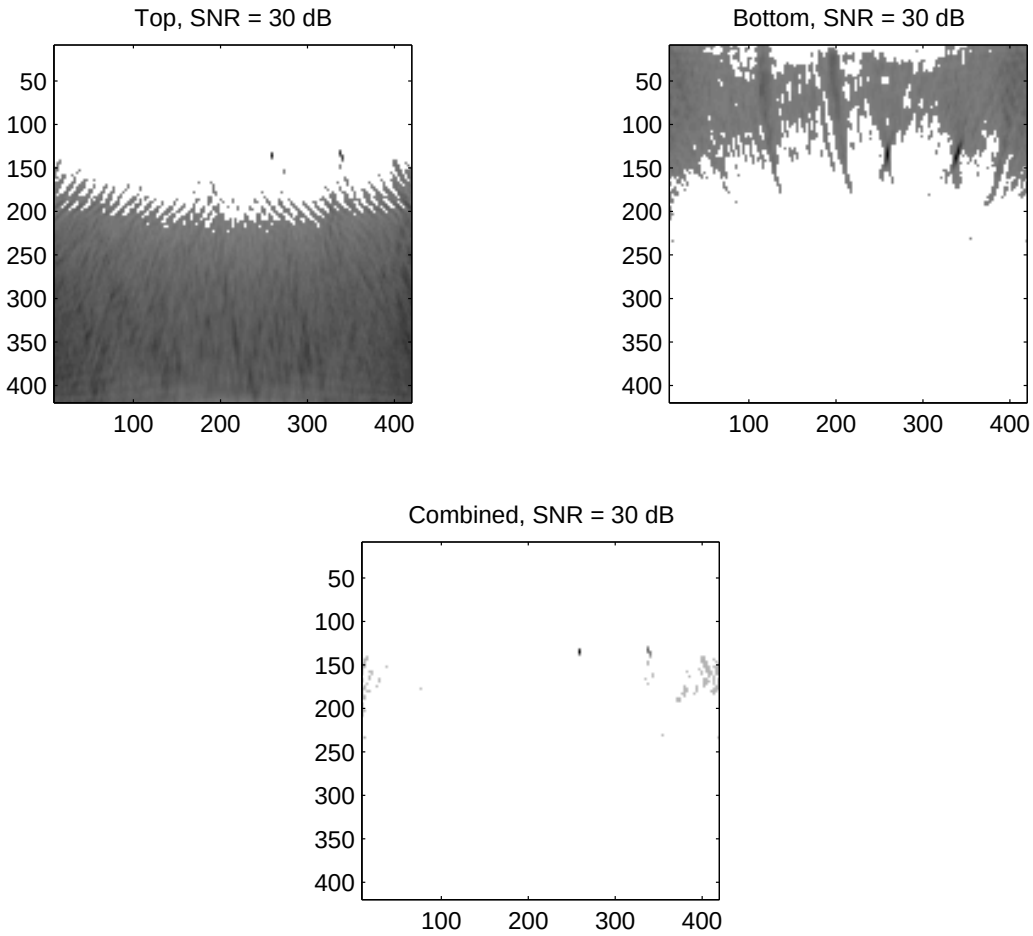

Combined thresholded pseudospectra at an SNR of 30 dB.

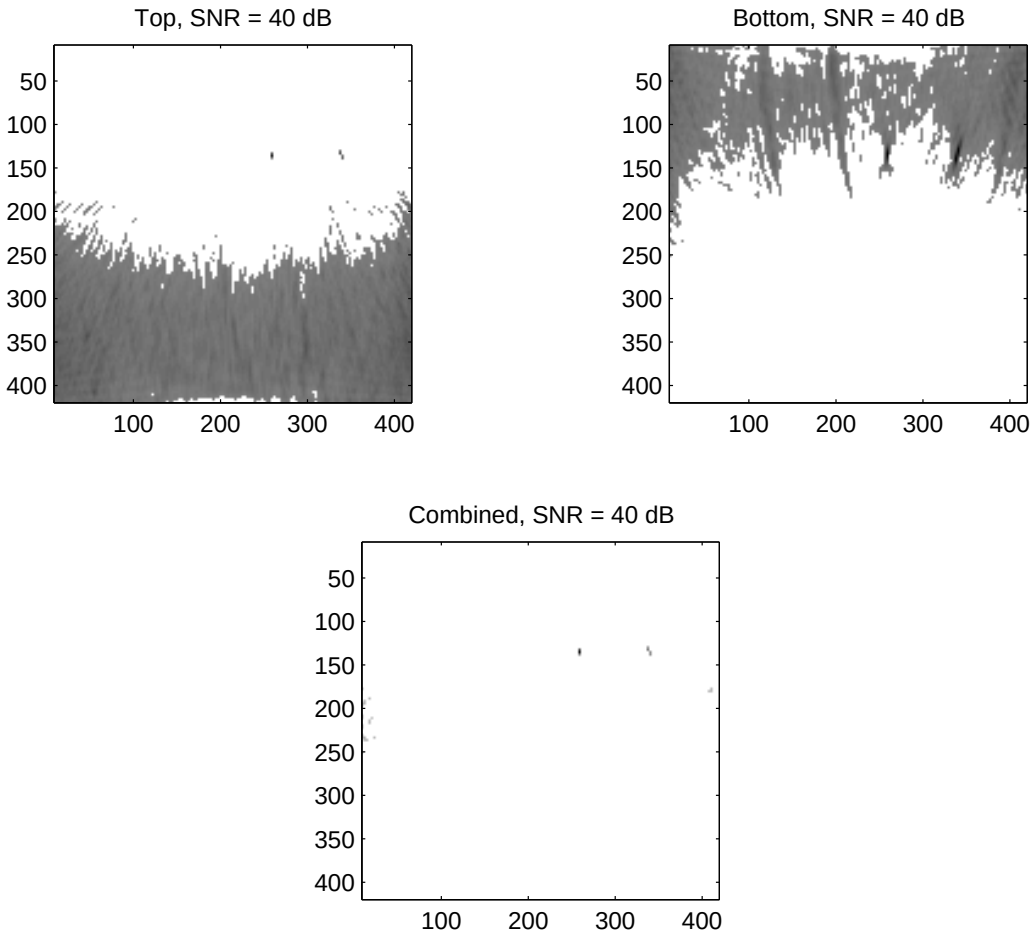

Combined thresholded pseudospectra at an SNR of 40 dB.

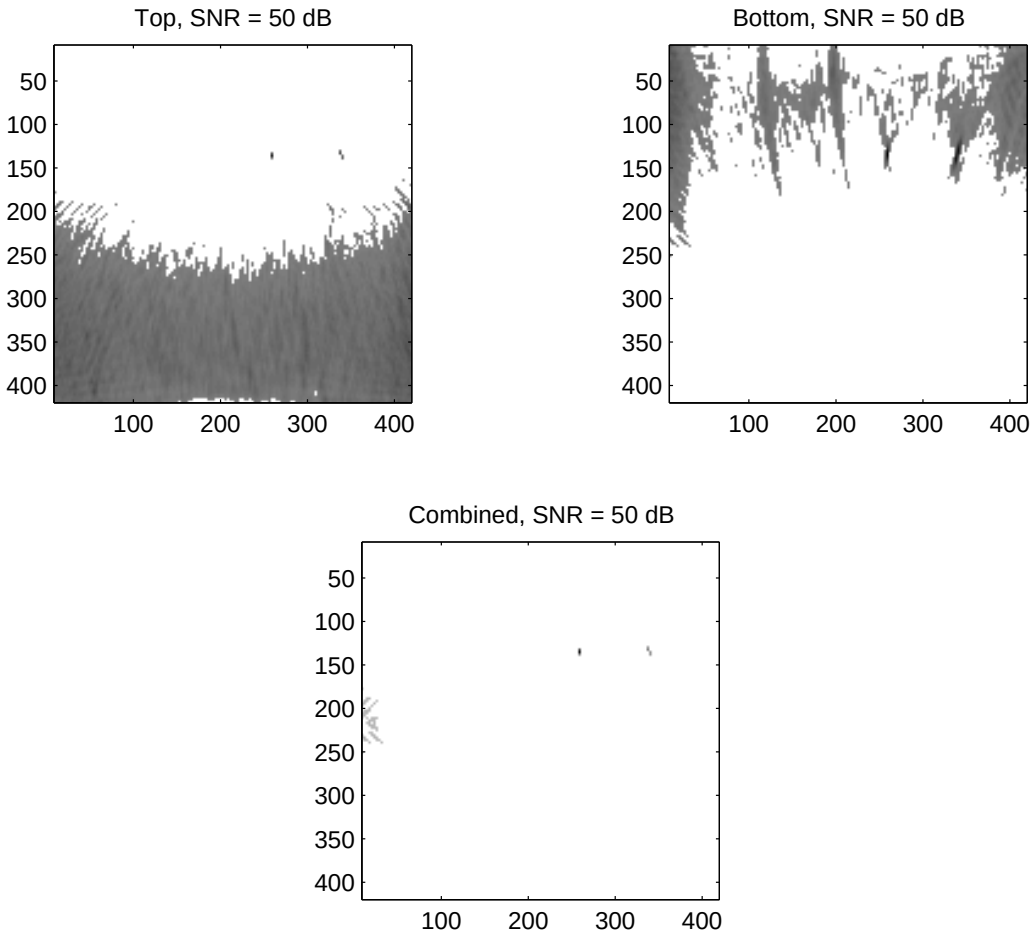

Combined thresholded pseudospectra at an SNR of 50 dB.

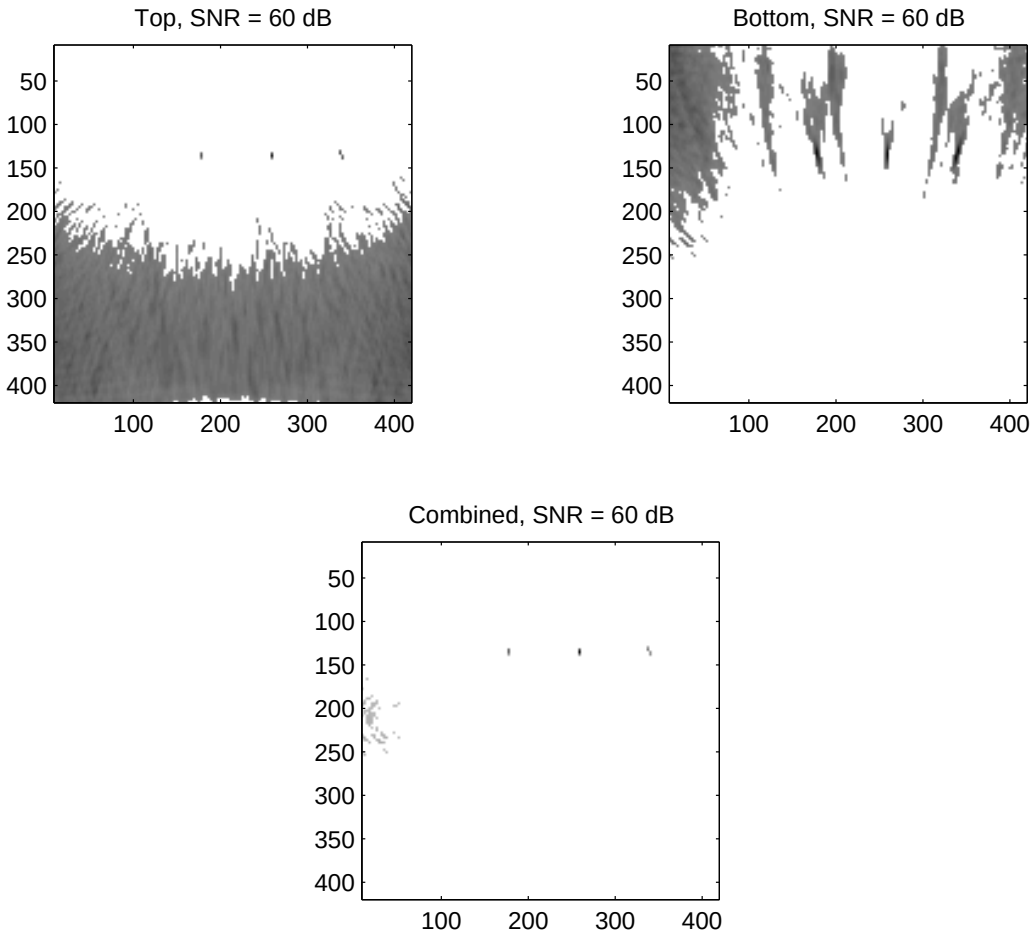

Combined thresholded pseudospectra at an SNR of 60 dB.

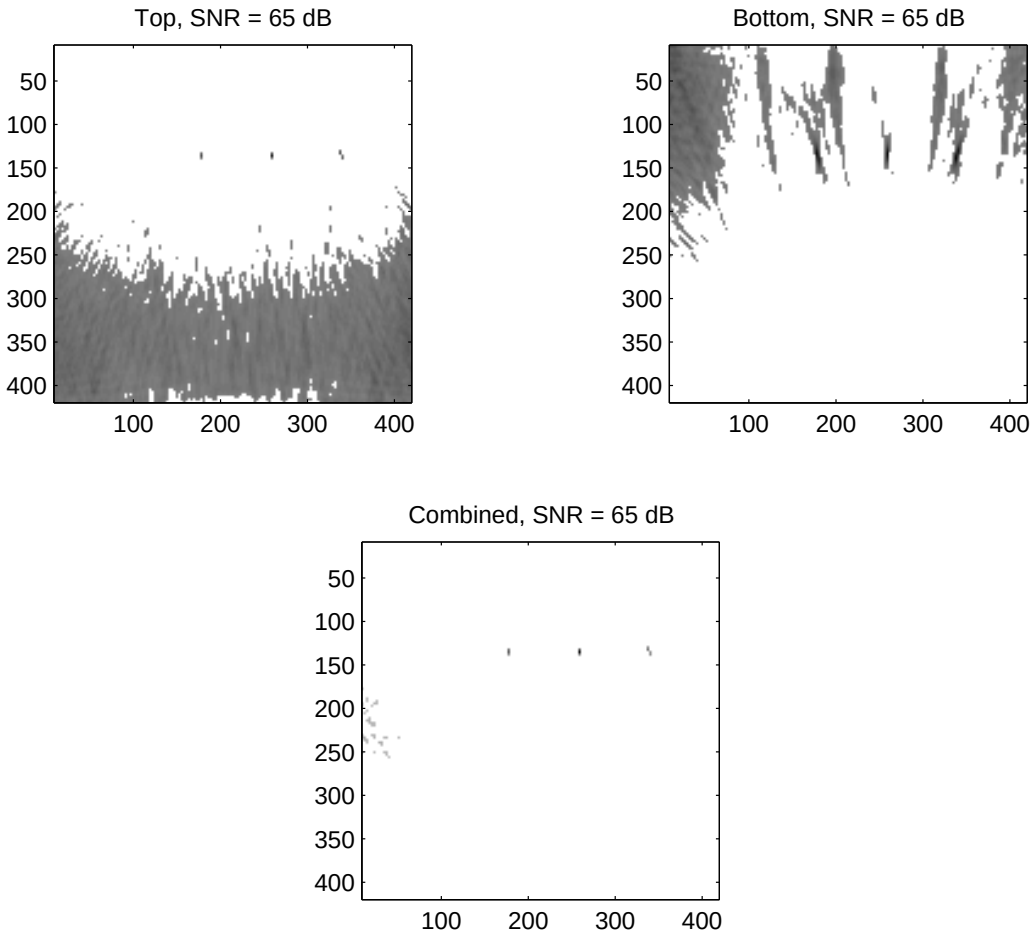

Combined thresholded pseudospectra at an SNR of 65 dB.

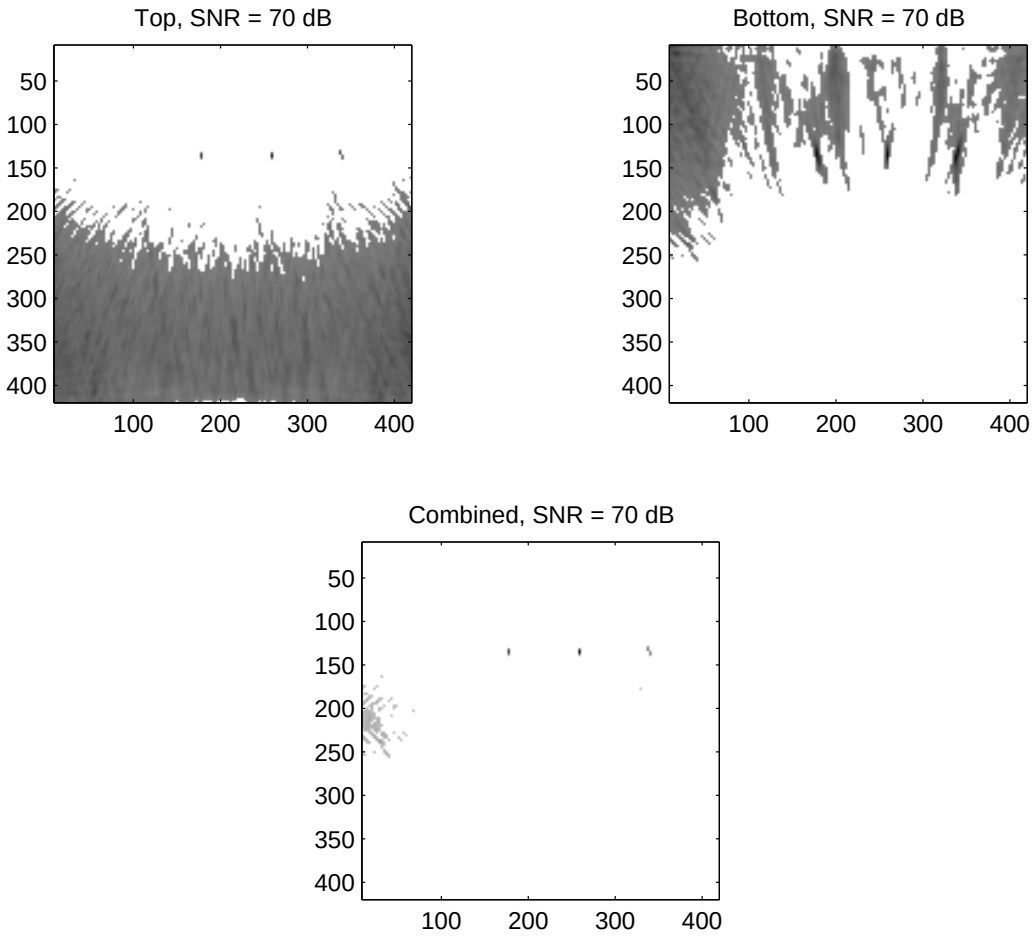

Combined thresholded pseudospectra at an SNR of 70 dB.

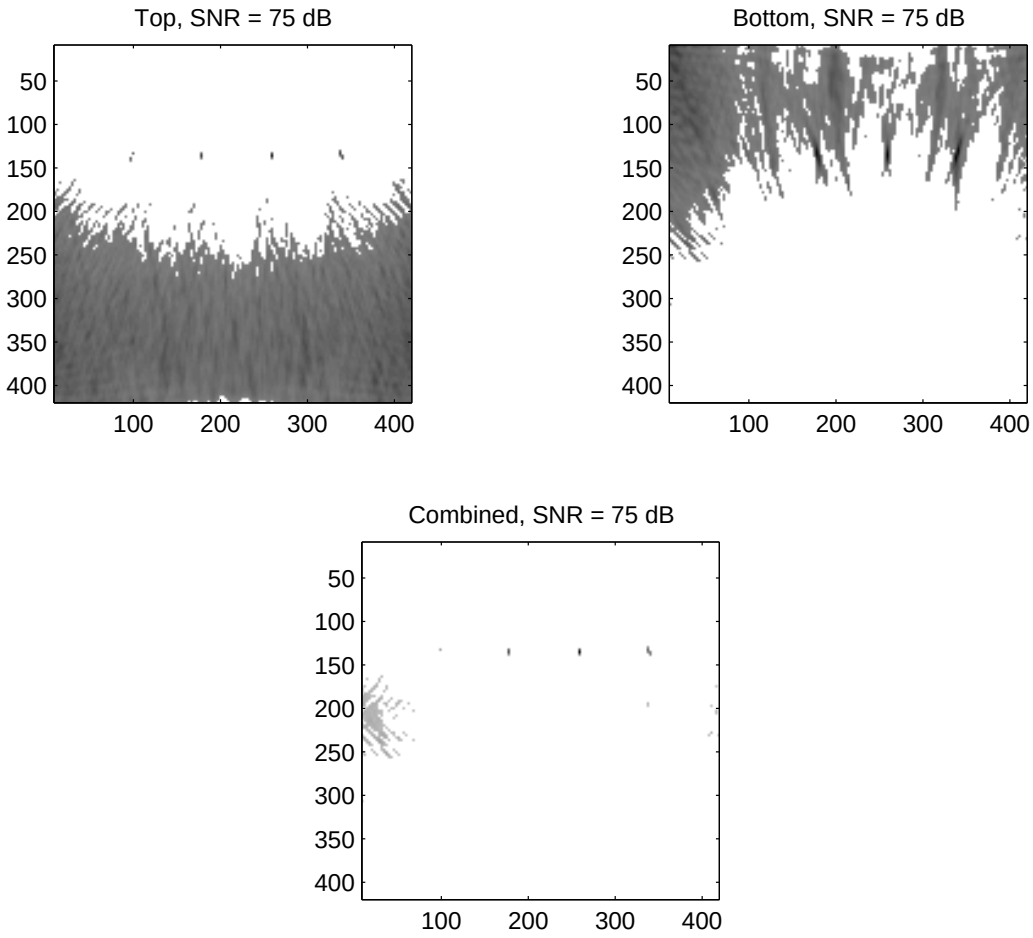

Combined thresholded pseudospectra at an SNR of 75 dB.

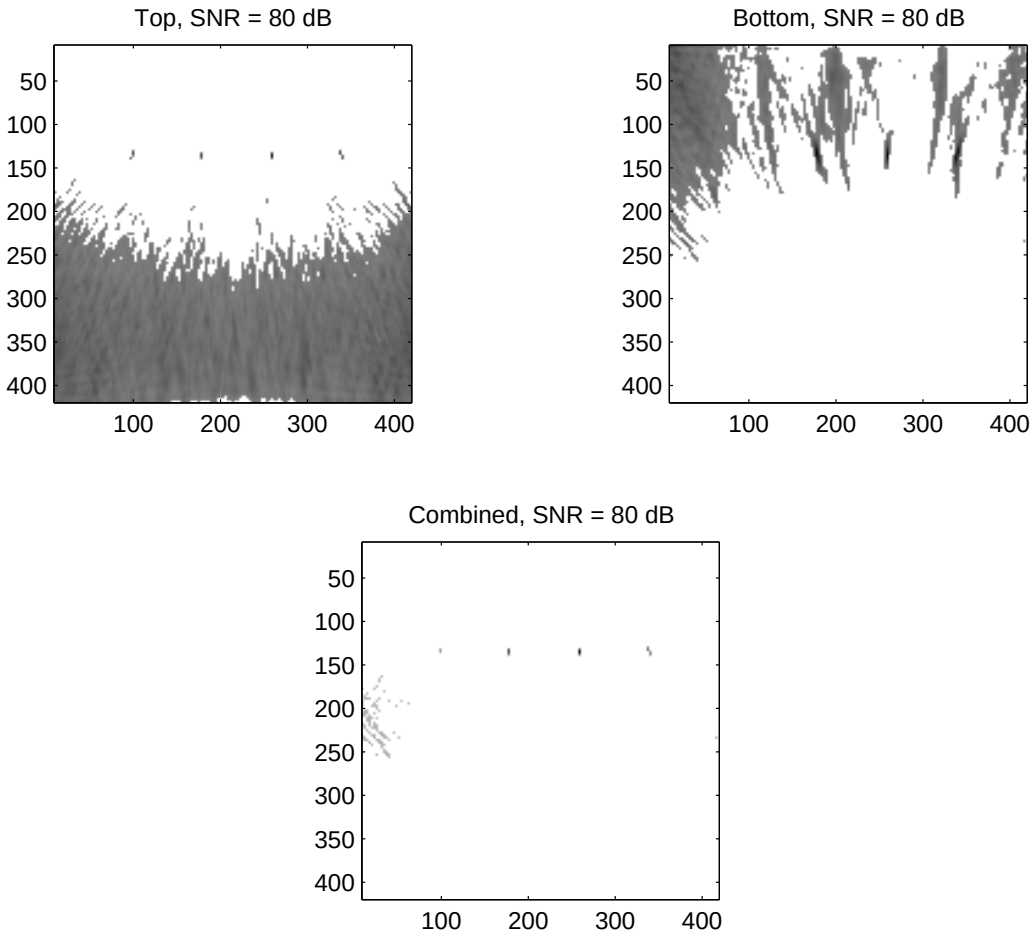

Combined thresholded pseudospectra at an SNR of 80 dB.

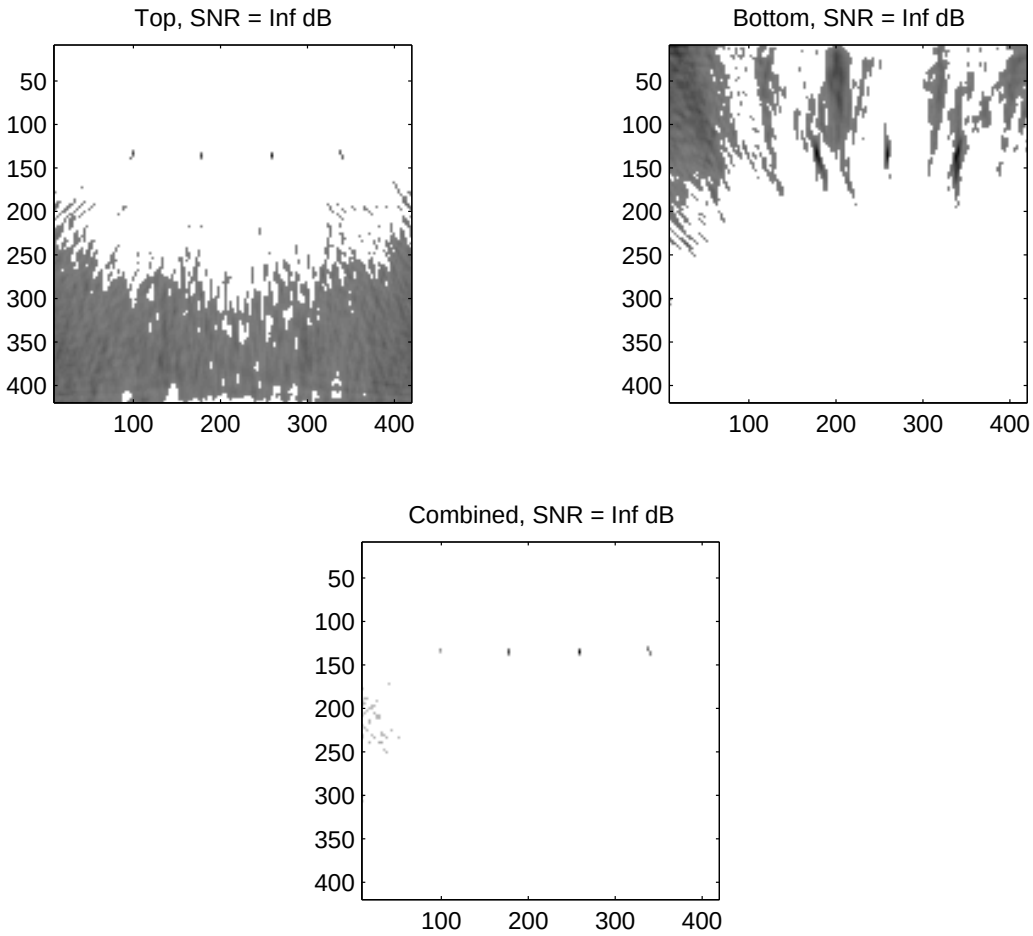

Combined thresholded pseudospectra at an SNR of ∞ dB.

References

[1] R. O. Schmidt. Multiple emitter location and signal parameter estimation. *IEEE Transactions on Antennas and Propagation*, **AP-34**(3):276–280, March 1986.

[2] S. K. Lehman and A. J. Devaney. Transmission mode time-reversal super-resolution imaging. *The Journal of the Acoustical Society of America*, **113**(5):2742–2753, May 2003.

[3] G. H. Golub and C. F. Van Loan. *Matrix Computations*. The Johns Hopkins University Press, 3nd edition, 1996. ISBN 0-8018-5414-8.

[4] M. Fink. Time-reversal of ultrasonic fields — Part I: Basic principles. *IEEE Transactions on Ultrasonics, Ferroelectrics and Frequency Control*, **39**(5):555–566, 1992.

[5] D. Cassereau and M. Fink. Time-reversal of ultrasonic fields — Part II: Theory of the closed time-reversal cavity. *IEEE Transactions on Ultrasonics, Ferroelectrics and Frequency Control*, **39**(5):579–592, 1992.

[6] C. Prada, J. L. Thomas, and M. Fink. The iterative time reversal process: Analysis of the convergence. *Journal of the Acoustical Society of America*, **97**(1):62–71, 1995.

[7] C. Prada, S. Manneville, D. Spoliansky, and M. Fink. Decomposition of the time reversal operator: Detection and selective focusing on two scatterers. *Journal of the Acoustical Society of America*, **99**:2067–2076, 1996.

[8] C. Prada, M. Tanter, and M. Fink. Flaw detection in solid with the D.O.R.T. method. *IEEE Ultrasonics Symposium Proceedings*, **1**:679–683, October 1997.

[9] L. L. Foldy. The multiple scattering of waves: I. general theory of isotropic scattering by randomly distributed scatterers. *Pysical Review*, **67**(3 & 4):107–119, February 1945.

[10] M. Lax. Multiple scattering of waves. *Reviews of Modern Physics*, **23**(4):287–310, October 1951.

[11] M. Lax. The multiple scattering of waves: II. the effective field in dense systems. *Physical Review*, **85**(4):621–629, February 1952.

[12] L. Tsang, J. A. Kong, K-H Ding, and C. O. Ao. *Scattering of Electromagnetic Waves: Numerical Simulations*. John Wiley & Sons, Inc., 2001. ISBN 0-471-38800-9.

[13] J. D. Jackson. *Classical Electrodynamics*. John Wiley & Sons, Inc., 3nd edition, 1999. ISBN 0-471-30932-X.

[14] G. Beylkin and M. L. Oristaglio. Distorted-wave born and distorted-wave rytov approximations. *Optics Communications*, **53**(4):213–216, March 1985.

[15] M. Born and E. Wolf. *Principles of Optics*. Cambridge University Press, 7th edition, 1999. ISBN 0-521-642221.